Draft version June 6, 2022
Typeset using LaTeX **twocolumn** style in AASTeX631

Establishing Dust Rings and Forming Planets within Them

Eve J. Lee [1,2] J. R. Fuentes [1] and Philip F. Hopkins [2]

[1] *Department of Physics and McGill Space Institute, McGill University, 3600 rue University, H3A 2T8 Montreal QC, Canada*
[2] *TAPIR, Mailcode 350-17, California Institute of Technology, Pasadena, CA 91125, US*

ABSTRACT

Radio images of protoplanetary disks demonstrate that dust grains tend to organize themselves into rings. These rings may be a consequence of dust trapping within gas pressure maxima wherein the local high dust-to-gas ratio is expected to trigger the formation of planetesimals and eventually planets. We revisit the behavior of dust near gas pressure perturbations enforced by a prescribed Gaussian forcing and by a planet in two-dimensional, shearing box simulations. We show analytically and numerically that when traveling through Gaussian-like gas perturbations, dust grains are expected to clump not at the formal center of the gas pressure bump but at least 1–2 gas scale heights away, so that with the non-zero relative velocities between gas and grains, drag-induced instabilities can remain active. Over time, the dust feedback complicates the gas pressure profile, creating multiple local maxima. These dust rings are long-lived except when forced by a planet whereby particles with Stokes parameter $\tau_s \lesssim 0.05$ are advected out of the ring within a few drift timescales. Scaled to the properties of ALMA disks, we find that if a dust clump massive enough to trigger pebble accretion is nucleated in our simulated dust rings, then such a clump would ingest the entire dust ring well within $\sim$1 Myr. To ensure the survival of the dust rings, we favor a non-planetary origin and typical grain size $\tau_s < 0.05$. Planet-driven rings may still be possible but if so we would expect the orbital distance of the dust rings to be larger for older systems.

1. INTRODUCTION

Planets are born in disks of gas and dust around a central star. Despite the vast progress in understanding the process of planet formation, the earliest phases remain unclear (e.g., Armitage 2018). In particular, the physical processes behind the growth of micrometer-sized dust particles into rocky bodies with sizes of thousands of kilometers remain unresolved.

One of the major obstacles in the coagulation of large solid bodies is the rapidity at which dust grains drift onto the central star due to aerodynamic drag (Whipple 1972; Weidenschilling 1977). In typical circumstellar disks around Sun-like stars, one-meter grain at one astronomical unit will be dragged to the inner disk edge within $\sim$200 years, approximately 4−5 orders of magnitude shorter than the typical disk lifetime (e.g., Chiang & Youdin 2010). While CO measurements reveal the gas disk to appear larger than the dust disk probed in radio continuum (e.g., Ansdell et al. 2018; Long et al. 2022), suggesting the grains undergo some degree of radial drift (e.g., Birnstiel & Andrews 2014)[1], the fact that these dust disks are extended to a few 10s of AU implies that the drift must be halted or delayed.

The classic calculation of radial drift derives from the assumption of a smooth gas disk. Substructures such as local pressure maxima within gas can act as traps collecting inflowing dust grains into ring-like structures (e.g. Pinilla et al. 2012). In fact, most of the bright protoplanetary disks imaged by the Atacama Large Millimeter/submillimeter Array (ALMA) shows concentric rings (ALMA Partnership et al. 2015; Andrews et al. 2018). What produces these pressure maxima is an open question (see e.g., Pinilla & Youdin 2017, for a review). Some suggestions include anticyclonic vortices in the gas (e.g., Lin 2014), edges of a gap carved out by perturbation from massive planets (e.g., Zhu et al. 2012), ice lines where volatiles condense (e.g., Brauer et al. 2008), and

Corresponding author: Eve J. Lee
evelee@physics.mcgill.ca

[1] We note however that the size discrepancy between the CO gas and the continuum dust emission may arise from different optical depths even in the absence of radial drift (Facchini et al. 2017; Trapman et al. 2019).

magnetic zonal winds (Dittrich et al. 2013). Although their origin is not well understood, since dust can collect within pressure traps, they have been proposed to be the regions where planetesimals and eventually planets form.

But can dust near and within pressure maxima be collected into sufficiently high density clumps to trigger secondary instabilities (e.g., streaming instability; Youdin & Goodman 2005; Johansen et al. 2007; Squire & Hopkins 2020) and/or collapse into bound planetesimals via self-gravity (Chiang & Youdin 2010; Simon et al. 2016; Gerbig et al. 2020)? Using 1D (radial) and 2D (radial-vertical) hydrodynamic simulations, Taki et al. (2016) found that once the dust grains collect within a pressure bump and reach a local dust-to-gas ratio of ~ 1, the dust backreaction destroys the pressure bump within ~ 500 orbital periods, suggesting that any long-lived gas/dust substructure as a viable site of planetesimal and planet formation requires continuous forcing (see however Onishi & Sekiya 2017 for a different view, who report that dust clumps of sufficiently high density can undergo gravitational instability but away from the disk midplane). With more sophisticated 3D hydrodynamic simulations of a gas pressure bump that is continuously reinforced including dust grains and dust self-gravity, Carrera et al. (2021) find that particles can clump to the Roche density (and therefore be expected to collapse into planetesimals) robustly and efficiently through the action of the streaming instability over multiple bump widths of their simulation box.[2]

Once these planetesimals coagulate within a dust ring, would they grow into massive bodies quickly enough to spawn gas giants? Morbidelli (2020) provided analytic arguments applying the theory of pebble accretion (Ormel & Klahr 2010; Lambrechts & Johansen 2012) to the B77 ring in the Elias 24 system in Dullemond et al. (2018). Under the assumption that the dust rings are created by a Gaussian pressure bump, Morbidelli (2020) concluded that a $0.1 M_\oplus$ seed mass can only grow up to $\lesssim 1 M_\oplus$ within these dust rings, mostly because of the large orbital distances where the dynamical timescales are long. The final core mass is even smaller if the seed mass is situated sufficiently far away from the center of the dust ring, where the dust density would be significantly lower.

In this work, we revisit the question of planet formation in dust rings. Our approach differs from and extends previous work in several important ways. First, while we focus primarily on 2D local, shearing box simulations, we investigate the dust-gas interaction in the $R-\phi$ (radial-azimuthal) plane rather than in the $R-z$ (radial-vertical) plane of the disk (i.e. we do not assume axisymmetry), under the assumption that the gravitational settling to the midplane occurs over much shorter timescale than any dynamical timescale on the plane of the disk (verified with a small number of explicit 3D simulations). Second, instead of initializing our simulation boxes with a pre-determined amount of dust particles distributed uniformly throughout the disk, we supply them over time from one side of the box, to simulate the drift of dust from the outer disk into a site of gas pressure bump, allowing (in principle) for an arbitrarily large buildup of dust mass as required in many models. Third, instead of simply imposing a pressure bump as an initial condition (where it would represent a purely transient effect and may not be able to act efficiently), we model it as an explicit acceleration term acting on the gas in two different ways: 1) a Gaussian pressure perturbation, and 2) a gravitational force, which mimics the presence of an embedded planet in the disk. Fourth, we consider a wide range of grain sizes and have surveyed a range of bump profile parameters. And fifth, we extensively consider the subsequent evolution of dense dust rings and bound clumps in simulated bumps, including comparison to observations of dust rings (allowing us to, in principle, separate different classes of bumps), and the ability of clumps to collapse under self-gravity (including shear and diffusion/turbulence effects).

This paper is organized as follows. Section 2 describes the model and numerical simulations used in this work. Further, we discuss the conditions for trapping particles in terms of the physical parameters of the bump and dust. In Sections 3 and 4 we investigate the dust distributions and trap efficiencies in simulations with bumps due to Gaussian forcing and due to a perturbation by a planet, respectively. In Section 5 we use the trap efficiencies from the simulations to estimate the expected mass evolution of the axisymmetric ring as well as the masses of the densest bound clumps within the rings we simulate (and compare to observational constraints). In Section 6 we investigate the ability of clumps to form and collapse under self-gravity, and the expected mass growth of the densest clumps after said collapse via pebble accretion. Finally, we summarize and conclude in Section 7.

[2] It is not surprising that the streaming instability is active away from the formal center of the pressure bump, since at the bump center, the dust-gas relative velocity would approach zero, likely deactivating any drag-induced instabilities.

2. PROBLEM & METHODS

2.1. *Problem Setup & Equations Solved*

We investigate the dynamics of dust grains near and at local pressure perturbations in a gas disk, where the perturbations are made either by Gaussian forcing (e.g., akin to ice condensations or zonal winds) or a tidal interaction with a planet. To concentrate on the local dynamics, we adopt the "shearing-box" approximation, i.e., calculations are performed on a small Cartesian patch of the disk defined in a rotating frame centered on $(R_0,\, \phi_0 + \Omega_0\, t, 0)$, where $\Omega_0 = \Omega(R_0)$ is the Keplerian orbital frequency at R_0. In this frame, the locally-Cartesian coordinates are $\mathbf{x} = (x,\, y,\, z) = (R - R_0,\, R_0(\phi - \phi_0) - R_0\Omega_0\, t,\, z)$. Expanding the equations of motion to $\mathcal{O}(|R - R_0|/R_0 \ll 1)$ gives the momentum equation for gas:

$$\frac{D\mathbf{u}}{Dt} = -\frac{\nabla P}{\rho} - 2\Omega_0\, \hat{\mathbf{z}} \times \mathbf{u} + 3\Omega_0^2\, \mathbf{x} - \Omega_0^2\, \mathbf{z} + \mathbf{a}_{\rm dust} + \mathbf{a}_{\rm bump}\,,$$

where $D/Dt = \partial/\partial t + (\mathbf{u}\cdot\nabla)$ is the Lagrangian derivative, ρ is gas density, P is gas pressure, $\mathbf{u}$ is gas velocity, $\mathbf{a}_{\rm dust}$ is the "back-reaction" acceleration from the force of gas drag on grains (defined below), and $\mathbf{a}_{\rm bump}$ is an acceleration due to an imposed force that models the pressure bump. For simplicity, in all our calculations we consider an inviscid gas described by an isothermal equation of state $P = \rho\, c_s^2$ with c_s the constant gas sound speed.

We introduce the Gaussian perturbation first. In the absence of dust "back-reaction" ($\mathbf{a}_{\rm dust} \to \mathbf{0}$), the gas has the equilibrium solution:

$$\bar{P} = P_0\, \left(1 + \delta_b\, e^{-x^2/2\, w_b^2}\right)\,, \tag{1}$$

$$\begin{aligned}\bar{\mathbf{u}} &= \left(0,\, -\frac{3}{2}\, x\, \Omega_0 - \eta\, U_K,\, 0\right)\,,\\ &= \left(0,\, -\frac{3}{2}\, x\, \Omega_0 - \Pi\, c_s,\, 0\right)\,,\end{aligned} \tag{2}$$

where $P_0 = P_0(R_0)$ is the unperturbed gas pressure evaluated at the center of the simulation box, $U_K \equiv \Omega_0\, R_0$ is the Keplerian velocity at the center of the simulation box, $\eta \equiv \eta(R = R_0) = -(\partial P_0(R)/\partial R)/(2\,\rho_0\,\Omega^2\, R) \equiv \tilde{\eta}\,(c_s/U_K)^2$ is the usual dimensionless pressure support parameter (defined at R_0 for the disk profile *without* a bump), $\Pi \equiv \eta\,(U_K/c_s) = \tilde{\eta}\,(c_s/U_K)$, δ_b is the dimensionless bump amplitude, and $w_b \equiv \tilde{w}_b\, H$ is the bump "width" in terms of the pressure scale height $H \equiv c_s/\Omega_0$. This gives

$$\mathbf{a}_{\rm bump} = 2\,\Pi\, c_s\, \Omega_0 \hat{\mathbf{x}} - \delta_b\, x\, \left(\frac{c_s}{w_b}\right)^2\, \left(1 + \delta_b\, e^{x^2/2\, w_b^2}\right)^{-1}\, \hat{\mathbf{x}}\,, \tag{3}$$

where $\mathbf{a}_{\rm bump}$ takes into account the acceleration due to the large-scale gas pressure gradient because the shear-periodic boundaries do not otherwise allow a pressure discontinuity between the $\pm\hat{\mathbf{x}}$ boundaries.

Next, we consider the gravitational perturbation by a planet of mass M_p located at $(x_p,\, y_p,\, z_p)$, whose gravitational field only acts on the gas (we turn off planet's gravity on dust grains so that we can isolate the effect of dust-gas dynamics in the presence of perturbations in the underlying disk gas).[3] In general, this planet will drive a wave (Goldreich & Tremaine 1980; Lin & Papaloizou 1986), and planets that are massive enough will carve out a gap (e.g., Rafikov 2002; Kley & Nelson 2012) in the vicinity of its orbit, creating a pressure bump located a few pressure scale heights away (Dong & Fung 2017). We write the bump acceleration as

$$\mathbf{a}_{\rm bump} = 2\,\Pi\, c_s\, \Omega_0 \hat{\mathbf{x}} - \nabla\Phi_p\,, \tag{4}$$

where Φ_p is the planet's gravitational potential

$$\Phi_p = -\frac{GM_p}{\sqrt{(x - x_p)^2 + (y - y_p)^2 + (z - z_p)^2 + r_s^2}}\,, \tag{5}$$

where we introduce a smoothing length parameter, $r_s = 0.1$ (in the unit of the disk scale height), to avoid the divergence of the planet's gravitational attraction.

In the shearing-box approximation, the momentum equation for dust particles is

$$\frac{d\mathbf{v}}{dt} = -\frac{\mathbf{v} - \mathbf{u}}{t_s} - 2\Omega_0\, \hat{\mathbf{z}} \times \mathbf{v} + 3\Omega_0^2\, \mathbf{x} - \Omega_0^2\, \mathbf{z}\,, \tag{6}$$

where $\mathbf{v}$ is the dust particle velocity and $d\mathbf{v}/dt$ is its Lagrangian derivative. We can thus write the acceleration on gas *from* dust grains (i.e. the "back-reaction" force on gas) as

$$\mathbf{a}_{\rm dust} \equiv \frac{1}{\rho}\, \int \frac{d\rho_{\rm d}}{d^3\mathbf{v}}\, \left(\frac{\mathbf{v} - \mathbf{u}}{t_s}\right)\, d^3\mathbf{v}\,, \tag{7}$$

where t_s is the stopping time of a *single* dust grain. We cannot assume that all grains at a given location move with the same velocity, so $d\rho_{\rm d}/d^3\mathbf{v}$ is the phase-space distribution of grains and $\rho_d \equiv \int (d\rho_{\rm d}/d^3\mathbf{v})\, d^3\mathbf{v}$ is the dust density. Since we are primarily interested in small grains, we assume an Epstein drag law such that the stopping time is given by

$$t_s \equiv \sqrt{\frac{\pi}{8}}\, \frac{\rho_{\rm grain}\, a_{\rm grain}}{\rho\, c_s}\, \left(1 + \frac{9\pi}{128}\, \frac{|\mathbf{v} - \mathbf{u}|^2}{c_s^2}\right)^{-1/2}\,, \tag{8}$$

(Paardekooper & Mellema 2006) where $\rho_{\rm grain}$ and $a_{\rm grain}$ are the *internal* grain density and radius, respectively.

[3] We verify with a limited set of simulations with planet's gravity on dust grains turned on that the overall qualitative behavior of the dust grains do not change.

Because t_s can depend on the local gas conditions (e.g. ρ), we define the usual dimensionless "effective Stokes number" $\tau_s \equiv \Omega_0\, t_s(\rho=\rho_0,\, P=P_0,\, R=R_0,\, |\mathbf{v}-\mathbf{u}|=0) \approx 0.63\, \rho_{\rm grain}\, a_{\rm grain}/\rho_0\, H$ where $\rho_0 = P_0/c_s^2$, in terms of the value of t_s evaluated for the equilibrium gas properties outside or absent the "bump". In steady-state *without* a bump and neglecting back-reaction on the gas, the dust equilibrium density is $\rho_d = \mu_0\, \rho_0$ (where μ_0 is the equilibrium dust-to-gas mass ratio) with the Nakagawa-Sekiya-Hayashi drift velocities (Nakagawa et al. 1986):

$$\bar{\mathbf{v}} = \bar{\mathbf{u}} - (2\,\tau_s,\, \tau_s^2,\, 0)\, \Pi\, c_s/(1+\tau_s^2)\,. \tag{9}$$

2.2. *Numerical Methods*

We integrate the equations described in Section 2.1 in GIZMO (Hopkins 2015),[4] using the Lagrangian "meshless finite mass" (MFM) method for the hydrodynamics (validated in e.g. Hopkins & Raives 2016; Hopkins 2016, 2017; Su et al. 2017). Grains are integrated using the "super-particle" method (see, e.g. Carballido et al. 2008; Johansen et al. 2009; Bai & Stone 2010; Pan et al. 2011), whereby the motion of each dust "particle" in the simulation follows equation (6), but each represents an ensemble of dust grains with similar properties. Numerical methods for the integration are described and tested in Hopkins & Lee (2016); Lee et al. (2017); Hopkins et al. (2020) with the back-reaction accounted for as in Moseley et al. (2019); Seligman et al. (2019), in a manner guaranteeing exact conservation.

We initialize a box of side-length $L_{\rm box}$, with shear-periodic boundary conditions for gas (Hawley et al. 1995) and $N_{\rm 1D,\,gas}^{D}$ resolution elements, where D is the number of dimensions. In the calculations using a Gaussian bump, the initial gas density and pressure obey the equilibrium solution for $\bar{P}$ (equation 1), whereas in the ones including a planet, the gas density is initially uniform within the box. In all our calculations, we set $L_{\rm box} = 6H$ to capture the bump without degrading the physical resolution. To find the optimal resolution for our study, we increase gradually $N_{\rm 1D,\,gas}$ and find convergence in the results when $N_{\rm 1D,\,gas} = 128$.

We set the mass of individual dust "super-particles" to be $m_{i,\,\rm dust} = 0.01\,\langle m_{i,\,\rm gas}\rangle = 0.01\, M_{\rm gas,\,box}/N_{\rm 1D,\,gas}^{D}$, where $M_{\rm gas,\,box}$ is the total mass of the gas in the box. Dust grains enter the right side of the box $+\hat{\mathbf{x}}$ (i.e. $R > R_0 + L_{\rm box}/2$) and exit the left side of the box $-\hat{\mathbf{x}}$ (i.e. $R < R_0 - L_{\rm box}/2$). For the inflow boundary at $+\hat{\mathbf{x}}$, we spawn new dust particles on a $D-1$ dimensional mesh (with $N_{\rm 1D,\,gas}^{D-1}$ elements) at a constant rate, set to the equilibrium drift $\bar{\mathbf{v}}$, such that the steady-state dust flux into the box is $\mathbf{F} = \langle\mu_0\rangle\, \rho_0\, \bar{\mathbf{v}}$ with $\langle\mu_0\rangle = 0.01$ (so that, *without* a bump, the steady-state dust-to-gas ratio in the box is $\langle\mu_0\rangle$).[5]

Since the time scale for vertical settling is short in comparison with the dynamical scales of interest in this work, we focus on 2D ($R-\phi$ or $x-y$) simulations. The 2D cases allow us to reach much higher resolution and are a plausible approximation for thin dust layers.

2.3. *Parameter Space*

2.3.1. *Gaussian bump*

In our idealized setup here, there are four *physically meaningful* parameters: τ_s, Π, $\tilde{w}_b$, and δ_b. Other parameters either scale out entirely from the problem (e.g. absolute values of ρ, c_s, R, Ω, etc.), or simply re-scale the rate of supply of dust, or are purely numerical parameters (e.g. dust and gas resolution, box size in units of H).

We note that three of the four meaningful parameters are narrowly constrained in terms of their values of interest and relevance to our problem. We expect $\Pi \sim 0.1$: much larger values ($\Pi \gtrsim 1$) imply the "disk" is actually a quasi-spherical hydrostatic object, while much smaller ($\Pi \lesssim 0.01$) would automatically mean the disk has Toomre $Q < 1$ *in the gas* and should fragment via gravitational instability. In all our simulations, Π is set to 0.05. Similarly we expect $\tilde{w}_b \sim 1$: if $\tilde{w}_b \gtrsim 1/\Pi \gg 1$ then the "bump" is not actually a bump, but a global disk structure, while if $\tilde{w}_b \lesssim \delta_b\,\Pi \sim 0.1$ the "bump" would immediately expand and/or explode because the implied pressure gradient acceleration actually becomes larger than the Keplerian gravitational force ($\sim U_K^2/R_0$). The bump amplitude and width δ_b and $\tilde{w}_b$ are further constrained by the requirement to trap dust initially, as we will show in Section 2.3.2 and Figure 1.

The most widely-variable parameter is therefore τ_s. For very large $\tau_s > 1$, the arguments below show that *no* physically-reasonable values of "bump" parameters can actually trap the dust (such grains are decoupled from the gas after all). So we focus on smaller grains, with $\tau_s \sim 0.01-1$. We do not explore smaller τ_s to keep the runtimes of our simulations reasonable.

[4] A public version of the code, including all methods used in this paper, is available at http://www.tapir.caltech.edu/~phopkins/Site/GIZMO.html

[5] We stress that the dust flux is a "nuisance parameter," as it only controls the rate of dust flowing into the bump, so changing it only changes the simulation time required for the bump to reach some interesting local dust-to-gas ratio.

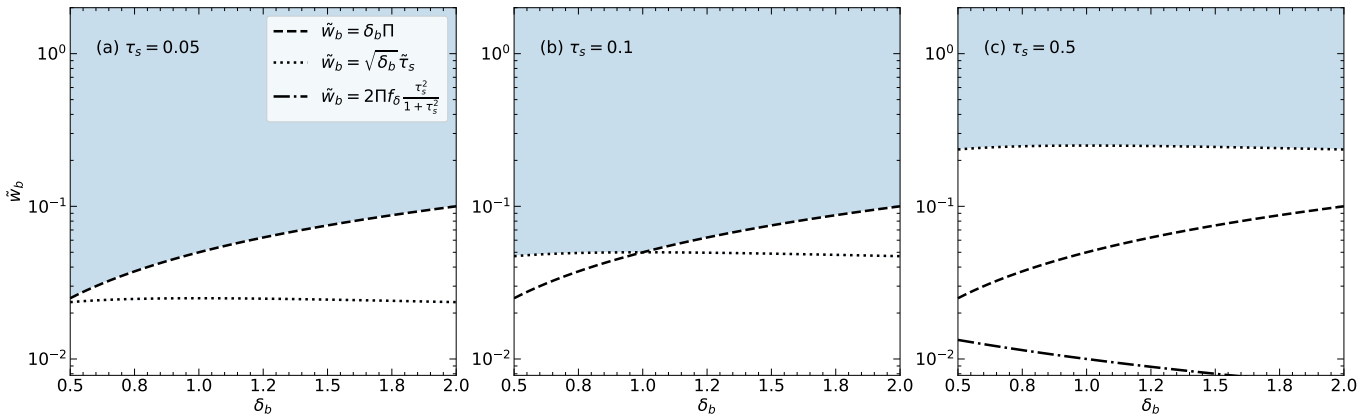

Figure 1. Parameter space constraints for the bump amplitude δ_b and width $\tilde{w}_b$, with $\Pi = 0.05$. The blue region represents the region of the parameter space that allows dust particles to be trapped by the bump, and the different lines denote the limits from the trapping requirements in Section 2.3.2. Since the size of the box is fixed to $L_{\rm box}/H = 6$, we limit the width of the bump up to a maximum of $\tilde{w}_b = 2$, to ensure the bump is contained within the box. The line corresponding to the constraint $\tilde{w}_b = \delta_b/3.3\Pi$ is above $\tilde{w}_b = 2$ and therefore not shown here.

2.3.2. *Trapping Requirements*

1) To be effectively a bump, the acceleration due to the Gaussian bump has to be greater than the background pressure gradient, particularly at one sigma from the peak where the acceleration is greater than at larger distances. This results in

$$\delta_b > 3.3\,\tilde{w}_b\,\Pi \quad \text{or} \quad \tilde{w}_b < \frac{\delta_b}{3.3\,\Pi}\,. \tag{10}$$

2) Dust particles need to slow down (on a time scale $\sim \tilde{t}_s$ "stopping time in the bump") before the equilibrium drift speed $v_{d,\,0}$ carries them "through" the bump (width w_b), i.e. $\tilde{t}_s \ll t_{d,\,0} \sim w_b/v_{d,\,0}$. Using $v_{d,\,0} \sim 2\,\Pi\,c_s\,\tau_s/(1+\tau_s^2)$, this requires

$$\tilde{w}_b \gtrsim 2\,\Pi\,\frac{\tau_s\,\tilde{\tau}_s}{1+\tau_s^2} = 2\,\Pi\,f_\delta\,\frac{\tau_s^2}{1+\tau_s^2} \tag{11}$$

where $\tilde{\tau}_s$ is the Stokes number "in the bump" with $\tilde{\tau}_s \approx \tau_s/(1+\delta_b) = f_\delta\,\tau_s$ in the Epstein regime.

3) The bump needs to "catch" grains accelerated by itself. As dust grains enter into the bump, assuming criteria above are met, grains accelerate up towards a new terminal velocity of $v_{d,\,b} \sim \tilde{t}_s\,\rho^{-1}\,\partial P_{\rm bump}/\partial R \sim 0.6\,\tilde{\tau}_s\,(\delta_b/\tilde{w})\,c_s$, crossing the peak (i.e. the "trap region" of width w_b) in a time $t_{d,\,b} \sim w_b/v_{d,\,b}$ which must be $< \tilde{t}_s$. Altogether, this gives

$$\tilde{w}_b \gtrsim \delta_b^{1/2}\,\tilde{\tau}_s\,. \tag{12}$$

We note that condition 3 is more stringent than condition 2 in the limit $\tau_s < 1$ unless $\delta_b^{1/2} \leq 2\pi\tau_s$. In the parameter space we explore, if condition 3 is met, condition 2 is automatically met.

4) For the bump to be stable (i.e., the acceleration by the bump pressure gradient does not exceed Keplerian acceleration), we must have:

$$\delta_b \lesssim 0.5\left(\frac{v_K}{c_s}\right)\tilde{w}_b \sim \frac{\tilde{w}_b}{\Pi}. \tag{13}$$

Based on these requirements, we choose $\delta_b/\tilde{w}_b = (0.5, 1.0, 2.0)$ and set $\tilde{w}_b = 1$. Note that with our choice of $\Pi = 0.05$ which is approximately the disk aspect ratio, our trapping requirements imply that these bumps may be Rossby-wave unstable (e.g., see Ono et al. 2016, their Table 2, case iv).[6]

2.3.3. *Planet-induced bump*

Pressure bumps can be created by planets that are massive enough such that the surrounding gas is pushed away from the planet's orbit. For inviscid disks, Lin & Papaloizou (1993) showed that gas surrounding the planet can be marginally stable against Rayleigh's rotational instability when the Hill radius of the planet, $R_{\rm Hill} = r(M_p/3M_\star)^{1/3}$, is comparable to the disk scale height, H, which yields the "thermal mass"

$$M_{\rm th} = \frac{2c_s^3}{3G\Omega_0}\,. \tag{14}$$

We vary the mass of the planet in the interval $0.1 - 2.7M_{\rm th}$, and find that pressure bumps form when $M_p \gtrsim$

[6] Ono et al. (2016) provide a fitting formula for the maximum Gaussian amplitude for stability against Rossby wave over two regimes: $0.02 \leq w_b/R \leq 0.05$ and $0.05 \leq w_b/R \leq 0.2$. At the boundary $w_b/R = 0.05$ (equivalent to our $\tilde{w}_b = 1$), the two fitting formula differ by at least an order of magnitude. While $\delta_b/\tilde{w}_b = 1.0$ and 2.0 are expected to be Rossby-wave unstable according to either of their criteria, $\delta_b/\tilde{w}_b = 0.5$ could be in the stable regime.

$0.5M_{\rm th}$. As our simulation boxes are focused on a small local patch of the protoplanetary disk, we keep the mass of the planet $M_p < 2.5M_{\rm th}$ to make sure the planet does not accrete significant amount of gas in the box. These constraints result in a narrow range of M_p, and we find that both the size of the bump and the dust dynamics do not change significantly so long as the pressure bumps are created. Therefore, we focus our discussion to $M_p = 2.25M_{\rm th}$.

We also fix the planet location at $x = -2H$ from the center of the simulation box so that the bump generated by the planet is contained in the box while giving enough room for dust particles to drift inward and interact with the bump.

3. CALCULATIONS WITH GAUSSIAN PRESSURE BUMPS

3.1. *Analytic expectations for dust distribution*

The classic expectation is that grains collect at the formal center of the pressure bump where the drift velocity is zero. This is true if the dust grains were originally uniformly distributed and then the gas was perturbed. In the following, we show analytically that if dust grains radially drift in, they collect some distance away from the formal center of the gas pressure bump.

From the continuity equation of dust in the radial direction x,

$$\frac{\partial \rho_{\rm d}}{\partial t} = -\frac{\partial(\rho_{\rm d} v_x)}{\partial x} \tag{15}$$

where $\rho_{\rm d}$ is the dust density (not to be confused with the material density of dust $\rho_{\rm grain}$), t is time, and v_x the relative radial velocity between the dust and the gas. Dividing equation 15 by $\rho_{\rm d}$ we obtain

$$\frac{\partial \ln \rho_{\rm d}}{\partial t} = -\frac{1}{\rho_{\rm d}}\frac{\partial(\rho_{\rm d} v_x)}{\partial x}. \tag{16}$$

Over some time $\Delta t = \Delta x / v_x$, the change in $\ln \rho_{\rm d}$ is

$$\Delta \ln \rho_{\rm d} \sim -\frac{\Delta t}{H}\frac{\partial v_x}{\partial \tilde{x}}, \tag{17}$$

where we assume $\partial_x \rho_{\rm d} \ll \partial_x v_x$ over Δt, and $\tilde{x} \equiv x/H$. Where the dust collect, $\Delta\rho_d$ is maximized whose location is determined by the inflection point of the dust radial velocity $d^2 v_x / dx^2 = 0$. We now show that this inflection point is not at the center of the bump. In steady state, the drift velocity is

$$v_x = \frac{\partial \ln P}{\partial \ln x}\left(\frac{c_s}{U_K}\right)^2 U_K \frac{\tau_s}{1+\tau_s^2}. \tag{18}$$

Both the background unperturbed disk and the "bump" (equation 1) contribute to the pressure gradient:

$$\frac{\partial \ln P}{\partial \ln x} = -2\Pi\left(\frac{U_K}{c_s}\right) - \frac{\tilde{x}^2}{\tilde{w}_b^2}\delta_b e^{-\tilde{x}^2/2\tilde{w}_b^2}\left[1+\delta_b\, e^{-\tilde{x}^2/2\tilde{w}_b^2}\right]^{-1}. \tag{19}$$

Substituting equation 19 into equation 18 and isolating the component due to the bump profile,

$$v_{\rm x,bump} \sim -\left[\frac{\tilde{x}^2}{\tilde{w}_b^2}\delta_b e^{-\tilde{x}^2/2\tilde{w}_b^2}\left(1+\delta_b\, e^{-\tilde{x}^2/2\tilde{w}_b^2}\right)^{-1}\right] \times \left(\frac{c_s}{U_K}\right)^2 U_K \frac{\tau_s}{1+\tau_s^2}. \tag{20}$$

whose inflection points lie at ± 0.8–$0.9\tilde{w}_b$ and ± 2.2–$2.4\tilde{w}_b$ for $\delta_b/\tilde{w}_b$ =0.5–2. Correcting the Stokes number for the bump profile (i.e., $\tau_s \rightarrow \tau_s/(1+\delta_b\, e^{-\tilde{x}^2/2\tilde{w}_b^2})$) yields inflection points of ± 0.9–$1.3\tilde{w}_b$ and ± 2.3–$2.6\tilde{w}_b$ for $\delta_b/\tilde{w}_b$ =0.5–2.

3.2. *Dust distribution*

Figure 2 shows radial profiles at different times of gas pressure, dust-to-gas mass ratio, and the radial velocity v_x of dust particles. As we expect, we find that dust particles distribute radially within the bump, and collect where the radial velocity inflects (the peaks in the dust-to-gas mass ratio coincide with the inflection points of v_x) rather than at the bump centre.

The radial velocity of dust from the simulation output deviates significantly from the expected analytic solution even at 300 orbital periods, likely because the solution is not in steady-state as was assumed in our analytic derivation. Nevertheless, the dust overdensity occurs where the radial drift slows down, like a traffic jam, and the sites of these traffic jams are displaced from the formal center of the pressure bump by at least w_b.

Over a long-term timescale ($\sim$ 3000 orbital periods), the radial distribution of the dust particles do not change substantially and remain localized (see Fig 3). Note that for the case $\delta_b/\tilde{w}_b = 0.5$ (the smallest bump amplitude) the dust particles more easily drift across and collect into multiple radial concentrations. We observe in all our simulations (including the ones for particles of $\tau_s \neq 0.1$, not shown here) the dust content is higher in the outer (right) edge of the pressure bump, where the dust-to-gas mass ratio increases to $\gtrsim$1. Dust-gas feedback causes a significant perturbation to the local gas pressure profile, and we observe the formation of non-axisymmetric clumps of dust particles, particularly at small τ_s, reflecting the effect of dust feedback that tends to trigger vortices in the dust ring (e.g., Huang et al. 2020).

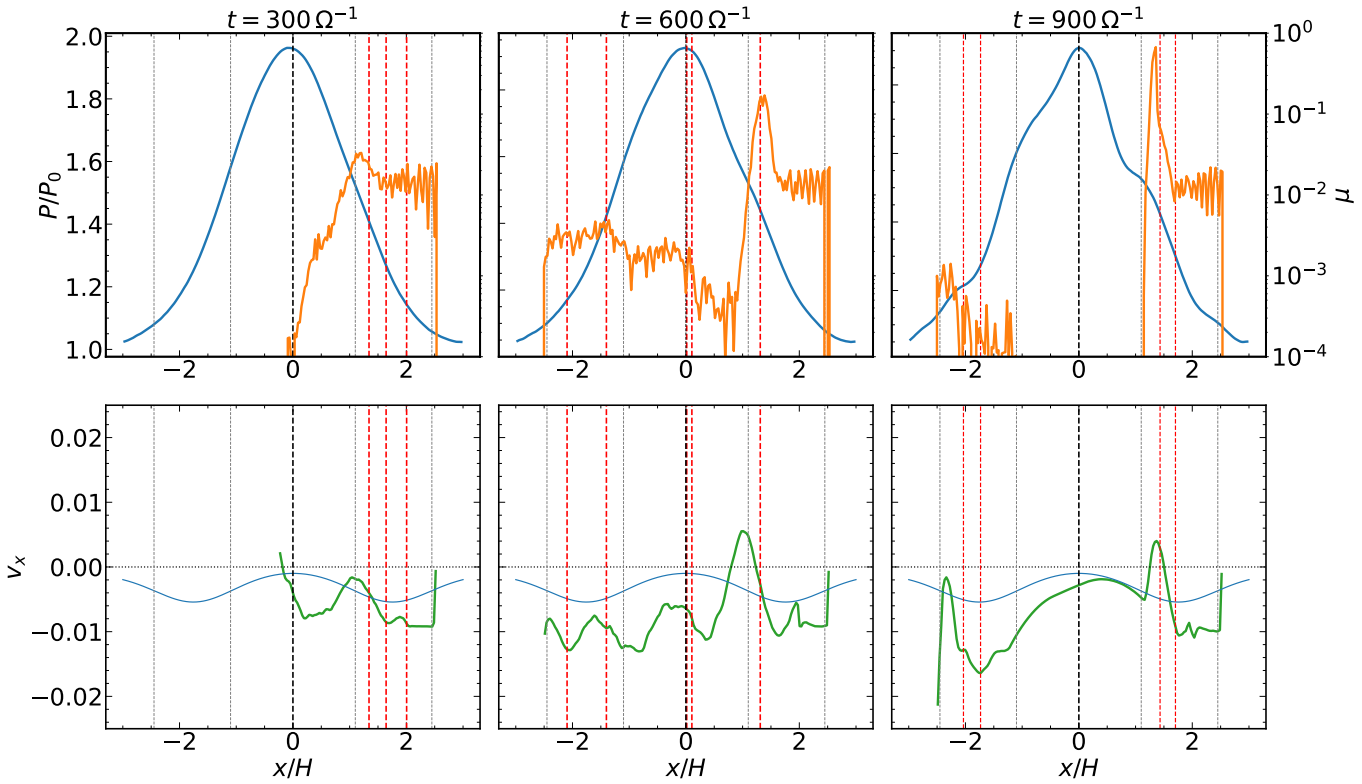

Figure 2. Top row: radial profile of gas pressure (P/P_0, blue) and dust-to-gas mass ratio (μ, orange). Note that for better visualization, we show the pressure profile using a linear scale on the left-vertical axis, whereas the dust-to-gas ratio is plotted using a logarithmic scale on the right-vertical axis. Bottom row: analytic expectation of the radial velocity of dust particles (equation 18), including correction by background pressure gradient (blue), and measured radial velocity from the simulation (green). Results are shown for particles of $\tau_s = 0.1$ interacting with a bump of initial profile $\delta_b = 1$, $\tilde{w}_b = 1$. The expected and measured inflection points of the radial velocity of dust delineated with the vertical dashed-lines in gray and red, respectively. The black dashed-line denotes the center of the pressure bump.

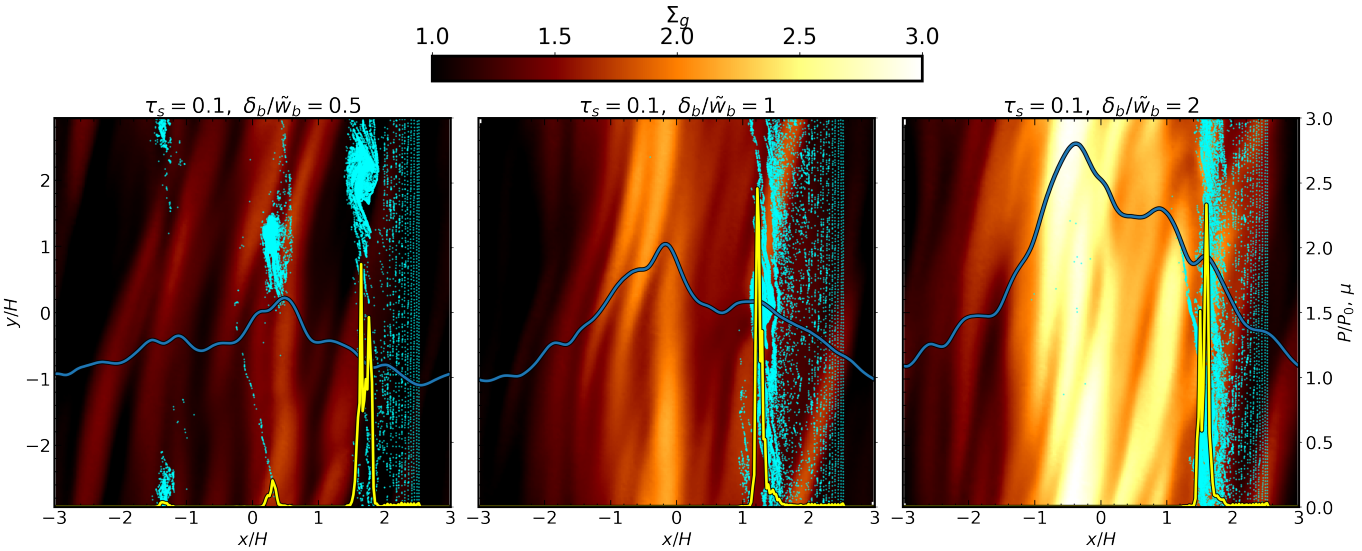

Figure 3. Snapshots of 2D gas density field (background) and the spatial distribution of dust particles (cyan points) at $t = 3030\,\Omega^{-1}$. The solid-lines correspond to radial profiles of the gas pressure (P/P_0 in blue) and dust-to-gas mass ratio (μ in yellow). Results are shown for runs at $\tau_s = 0.1$. Left, middle, and right panels show results for initial gas pressure bumps of amplitude $\delta_b/\tilde{w}_b = 0.5$, 1, and 2, respectively. All panels share the same color scale.

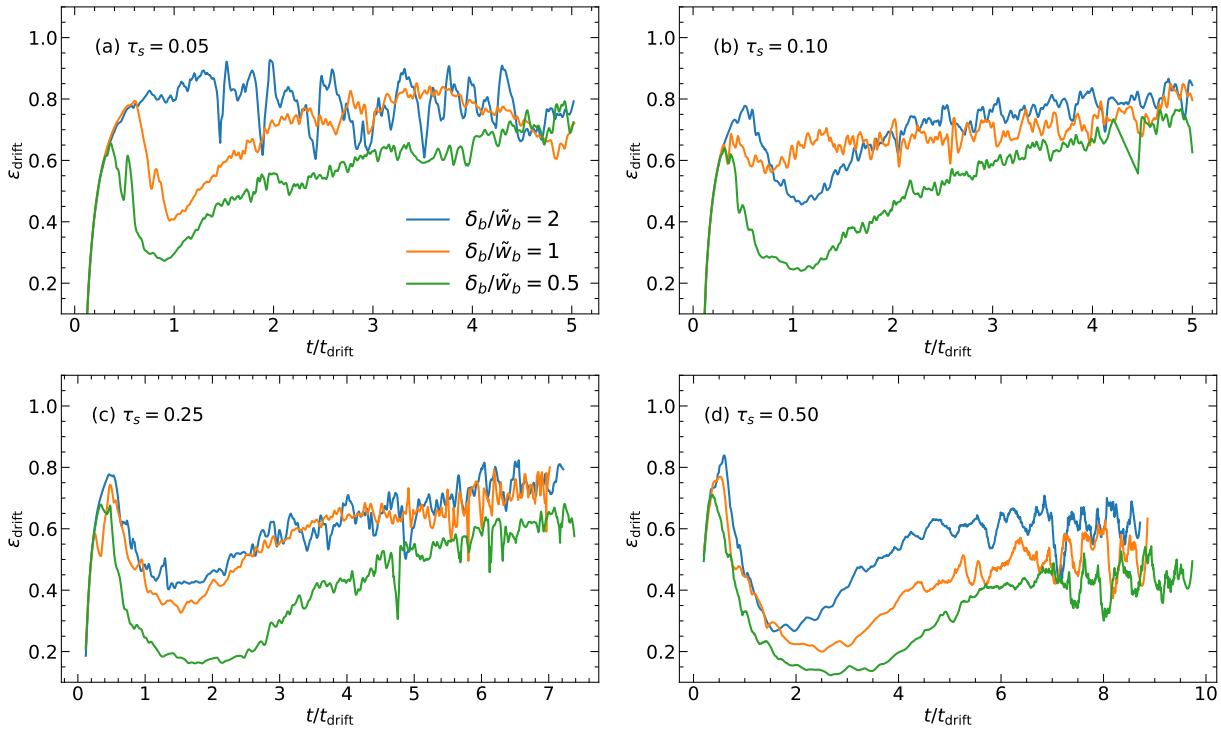

Figure 4. Trap efficiency $\epsilon_{\rm trap}$ as a function of time for different τ_s and initial Gaussian bump profiles. Results are shown up to the end of their simulation runs. All our Gaussian-forced rings lose some particles at ∼1–4 drift times after which the trap efficiency recovers.

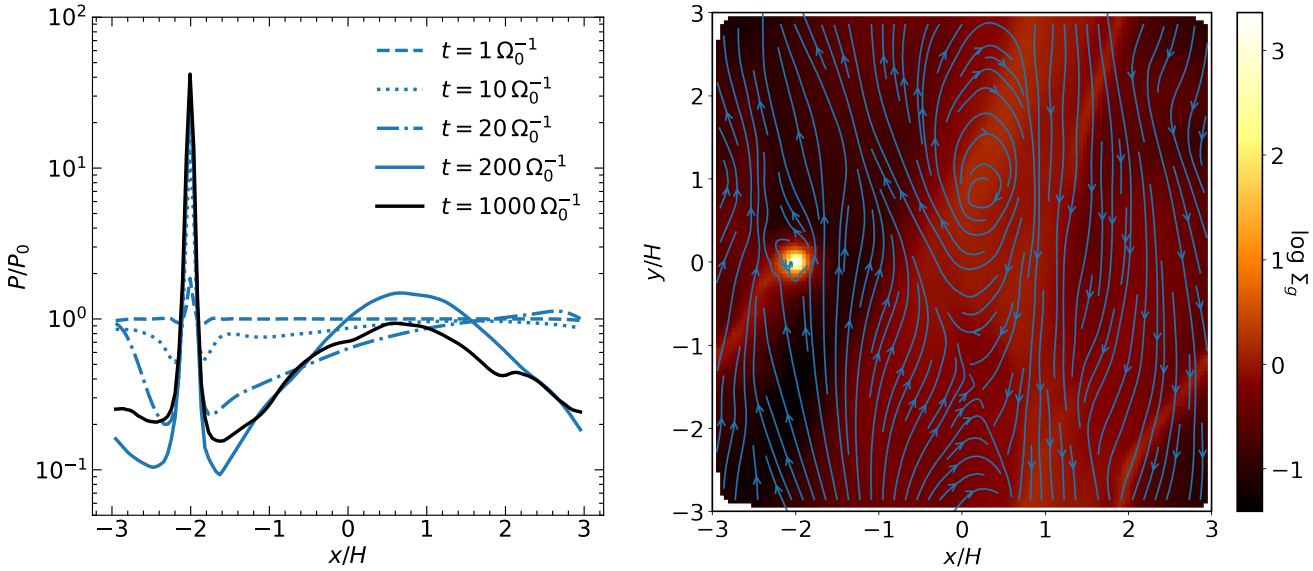

Figure 5. Left: radial distribution of the gas pressure, P/P_0, for $M_p/M_{\rm th} = 2.25$ at different times. The planet of mass $2.5M_{\rm th}$ is located at $x = -2H$. Note that a Gaussian bump external to the planet's orbit establishes after a few hundred orbital times. Right: 2D field of the gas density with streamlines of the gas velocity field (blue lines). We observe the formation of vortices which is expected given that the pressure bump created by the planet is formally unstable to Rossby wave instability. All our numerical experiments show the same qualitative behavior.

3.3. *Trap efficiency*

We calculate the efficiency of the trap $\epsilon_{\rm trap}$ as the ratio between the number of dust particles inside the "dust-rich bands" and the cumulative number of particles supplied to the bump at a given time. We define a dust-rich band by fitting a Gaussian function to the radial distribution of dust grains, centred at the peak of such distribution. When there are multiple peaks, we force the fit to the outer peak as this peak eventually grows to overwhelm all other peaks. Then, we count the number of particles within two Gaussian standard deviations in the dust-rich region to estimate $\epsilon_{\rm trap}$.

Since we want to compare results for particles of different τ_s, which are supplied to the box at a different rate, in the following we present results at times normalized by the radial drift time across the box

$$t_{\rm drift} \sim \left(\frac{N_H}{2\Pi}\right)\left(\frac{1+\tau_s^2}{\tau_s}\right)\Omega^{-1}\,, \tag{21}$$

where N_H is the number of pressure scale heights ($N_H = 6$ in our simulations). For particles of $\tau_s = (0.05,\, 0.1,\, 0.25,\, 0.5)$, the radial drift times are $t_{\rm drift} \approx (1203,\, 606,\, 255,\, 150)\,\Omega^{-1}$, respectively.

Figure 4 shows that the time evolution of $\epsilon_{\rm trap}$ exhibits a significant amount of scatter, as both the location and the width of the dust ring changes from time to time as the gas profile is perturbed. On average, we identify some trends between $\epsilon_{\rm trap}$, $\delta_b/\tilde{w}_b$, and τ_s. Narrower bumps (larger $\delta_b/\tilde{w}_b$) trap particles more efficiently due to the larger force exerted by the bump. With the exception of $\delta_b/\tilde{w}_b = 2$ and $\tau_s = 0.05$, we observe a significant leaking of particles at early times ($t/t_{\rm drift} < 1$), larger τ_s being the most affected. Such particles are expected to drift in faster and so with an identical pressure bump profile, they are the hardest to capture (see Section 2.3.2). As more dust collects at the site of traffic jam, perturbation to the gas by dust feedback enhances even more the gradient of dust radial velocity (see Figure 2) and $\epsilon_{\rm trap}$ recovers within 2–4 drift times and eventually reach ~ 0.4–0.8.

4. CALCULATIONS WITH PLANET-INDUCED PRESSURE BUMP

4.1. *Gap formation and pressure bump*

With the introduction of gravity from a thermal mass object, some of the surrounding gas is rapidly accreted onto the planet and density waves are excited in the gas, pushing the gas away toward the radial boundaries. This process results in a density gap around the planet's orbit and a pile up of gas a few H away from the planet (see left panel in Figure 5). The gas responds to the initial perturbation on a short time and equilibrates after a few hundred orbital times. We note that the planet-induced pressure bump resembles a Gaussian. By fitting a Gaussian function to the planet-induced bump, we find $\delta_b = 1.44$ and $\tilde{w}_b = 0.96$, strong enough to meet our trapping conditions (Section 2.3.2) and likely Rossby-wave unstable (Ono et al. 2016), creating vortices near the bump (see the gas streamlines in right panel of Figure 5).

We note that after about 20 orbital times, the gas pressure at the location of the planet remains roughly constant. To make sense of this time scale, we estimate analytically the characteristic time for the accretion process. For 2D accretion, the gas mass accretion rate is given by

$$\dot{M} \sim R_{\rm acc,g}\Sigma_{\rm g} v_{\rm acc,g}\,, \tag{22}$$

where $R_{\rm acc,g}$ and $v_{\rm acc,g}$ are the accretion radius and velocity, respectively, and $\Sigma_{\rm g}$ is the gas surface density. For $M_p \sim M_{\rm th}$, the Hill radius of the planet becomes smaller than its Bondi radius, and therefore $R_{\rm acc,g} \sim R_{\rm Hill}$. As the ambient gas flow approaches $R_{\rm acc,g} \sim R_{\rm Hill}$, it will accelerate to the shear velocity at the Hill radius: $v_{\rm acc,g} \sim \frac{3}{2}\Omega R_{\rm Hill}$. The gas accretion rate onto the planet is then

$$\dot{M} \sim \frac{3}{2} R_{\rm Hill}^2 \Sigma_{\rm g}\Omega\,. \tag{23}$$

As the planet orbits the star, it sweeps up the gas material around on a time scale $t_{\rm sweep} \sim M_{\rm av}/\dot{M}$, where $M_{\rm av} = \Sigma_{\rm g} r R_{\rm Hill}$ is the mass available to the planet at orbital distance r. Noting that $R_{\rm Hill} = fH$, where $f = (2M_p/9M_{\rm th})^{1/3}$, and recalling that for a thin disk $\Pi \sim c_s/U_K \sim H/r$, we obtain

$$t_{\rm sweep} \sim \left(\frac{M_p}{M_{\rm th}}\right)^{-1/3} \Pi^{-1}\Omega^{-1}\,. \tag{24}$$

As a check, for $M_p/M_{\rm th} = 2.25$, and $\Pi = 0.05$, equation 24 gives $t_{\rm sweep} \sim 15\,\Omega^{-1}$ consistent with the results in Figure 5.

4.2. *Dust distribution*

Figure 6 visualizes the radial distribution of the gas pressure and dust-to-gas mass ratio, as well as the 2D spatial distribution of dust particles. We find that the morphology of the dust band is strongly dependent on τ_s. For $\tau_s = 0.05$, any dust concentration we see is transient and is advected away following the gas flow onto the planet over just just one drift time. We also observe more complex geometry of the dust ring with signatures of vortices, likely following the vortices in the gas streamlines (Figure 5). In general, the gas pressure bump is constantly deformed not just by the dust feedback but also by the density waves driven by the planet.

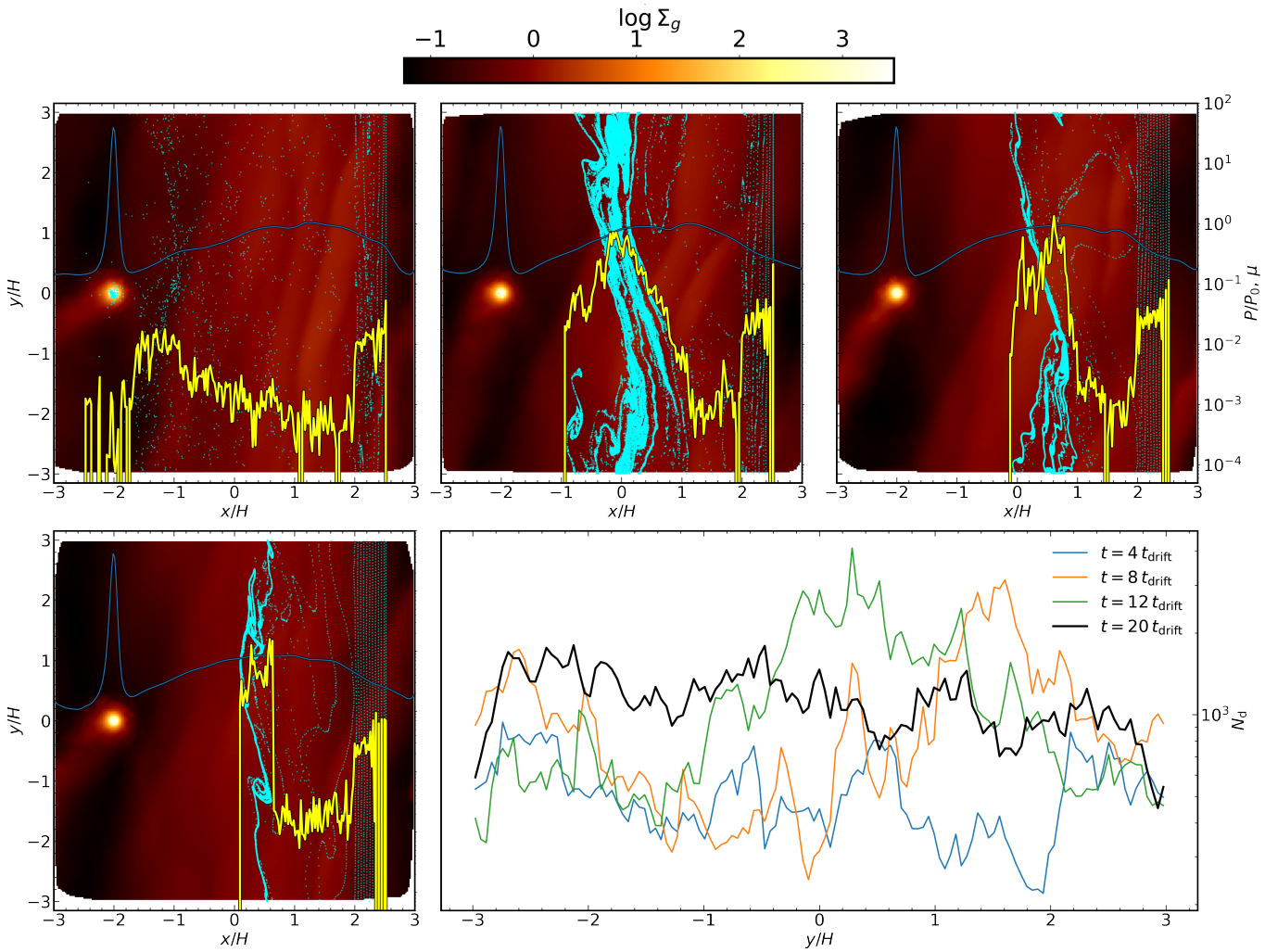

Figure 6. Top row + bottom left panel: snapshots of 2D gas density field (background) and the spatial distribution of dust particles (cyan points) for $\tau_s = 0.05$ (top left), 0.10 (top middle), 0.25 (top right), and 0.50 (bottom left), shown here at $5t_{\rm drift}$. In all cases, the pressure bump was created by a planet of mass $M_p = 2.25M_{\rm th}$, and the planet's location is $(-2H, 0)$. The solid-lines correspond to radial profiles of the gas pressure (P/P_0 in blue) and dust-to-gas mass ratio (μ in yellow). The snapshots are shown at $t = 5\,t_{\rm drift}$. Bottom right: particle number distribution along the azimuthal coordinate (y/H) for $\tau_s = 0.1$. While the particles show non-axisymmetric pattern, they evolve towards a more axisymmetric distribution. We observe the same qualitatiebehavior for particles of larger τ_s.

The complex morphology of gas streamlines begets the complex morphology of dust bands.

For particles of $\tau_s = 0.05$, the pressure bump is an ineffective barrier. We observe the particles going through the bump and arriving at the location of the planet, from where they are constantly kicked out of the box by gas outflows. For $\tau_s = 0.1$, 0.25, and 0.5, we find that particles become trapped slightly off-center of the pressure bump, similar to the runs using a Gaussian forcing. However, the dust-rich regions are located near the inner (right) edge of the bump instead. We find that $\mu \sim 1$ in these locations and that the radial extent of the dust-rich region becomes smaller for larger τ_s as larger particles are more decoupled from the gas and therefore more resilient against advective outflow from the gas bump. We note that in spite of the initial vortex formation in dust rings, over time, the dust concentrations transition to axisymmetric rings (see the bottom right panel of Figure 6).

4.3. *Trap efficiency*

Like the Gaussian forcing case, we compute $\epsilon_{\rm trap}$ as the ratio between the number of dust particles inside the dust-rich bands (defined using Gaussian fits) and the cumulative number of particles spawned and drifted in from the edge of the simulation box. Recall that for the runs with Gaussian forcing, the efficiency of the trap $\epsilon_{\rm trap}$ decays at early times ($t/t_{\rm drift} \lesssim 1$) and on the long term, it slowly recovers and saturates toward a constant

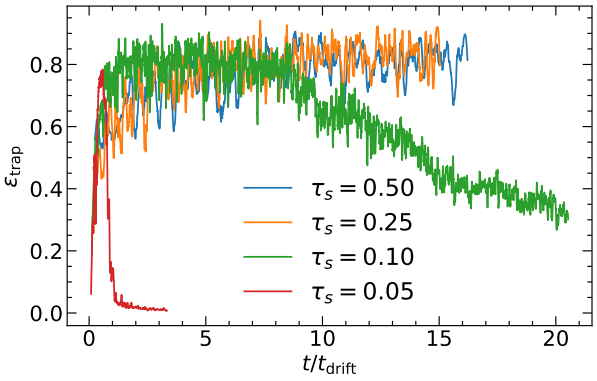

Figure 7. Trap efficiency $\epsilon_{\rm trap}$ of planet-driven ring as a function of time. Planet mass is fixed to $M_p = 2.25 M_{\rm th}$. At the lowest τ_s, the dust ring is advected away within $\sim$1 drift time and we also see a gradual loss of particles from the ring of particles at $\tau_s = 0.10$.

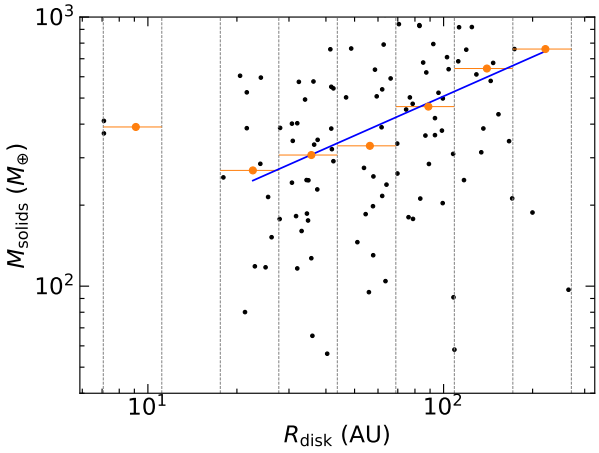

Figure 8. Disk dust mass and radius estimates for Class 0 and I sources (Tobin et al. 2020, black circles) where we take the mass measurements from VLA and the size measurement from ALMA (see text for the rationale). We binned the data over $R_{\rm disk}$ (the vertical lines denote the edge of each bin) and take the mean value of each bin as a representative value of $M_{\rm solids}$ (orange dots). The blue line is a power law fit to the last six bins (equation 25).

value. By contrast, in planet-induced bumps, $\epsilon_{\rm trap}$ starts at $\sim$0.8 and either decreases with time or stays constant (at least for the duration of our simulations), depending sensitively on τ_s (see Figure 7). The high initial trapping efficiency comes from vortices acting as effective dust traps.

At lower τ_s (especially for $\tau_s = 0.05$), the particles, being coupled to the gas flow, are eventually advected out of the pressure bump before they can collect into thin rings. We find this behavior persists when we turn off dust feedback—in fact, dust feedback aids the stabilization of dust rings against advection—and we did not observe any noticeable difference in the morphology of planet-induced pressure bump when we increased (or decreased) the resolution from our fiducial 128^2 particles, suggesting the effect is not dominated by e.g. numerical viscosity. For these small τ_s, the dust band leaks out more easily when we turn on planet gravity on dust grains as the grains are attracted to the planet on top of being advected out following the gas flow. As $\tau_s < 0.1$ grains have been shown to collect into thin rings under the presence of a planet both sub- and super-thermal over thousands of orbital times in global disk simulations with different numerical schemes (e.g., Dong et al. 2017), we suspect that the transient ring we observe may be a feature of our local shearing box simulation, which will need to be verified (in the future) using 2D global simulations with GIZMO.

For particles of $\tau_s = 0.1$, the bump is able to trap dust and $\epsilon_{\rm trap}$ remains high until $t \approx 8\, t_{\rm drift}$. Afterwards, we find that $\epsilon_{\rm trap}$ decays with time until the system reaches an equilibrium between the number of particles that escape from the bump and the number of particles supplied to the bump. Finally, for particles of $\tau_s = 0.25$ and 0.5, we do not observe a significant particle leak, and the efficiency of the trap remains high and stable over long time-scales.

5. INITIAL MASS RESERVOIR AND RINGS

We now evaluate the amount of solid mass that could be trapped in the rings we simulate and compare to the inferred ring masses in ALMA disks. The initial solid mass reservoir is inferred from the mass and radius measurements of Class 0/I disks in the Orion cluster that are detected with both ALMA (0.87 mm) and the VLA (9 mm), reported by Tobin et al. (2020). Following the procedure of Chachan et al. (2022), we take the dust masses from VLA observations as disks are expected to be more optically thin at longer wavelengths (and so they are closer to the true masses). Disk sizes are taken from ALMA measurements as protoplanetary disks tend to appear smaller at longer wavelengths (e.g., Tazzari et al. 2016) which may be an effect of different optical depths (Tripathi et al. 2018). By taking the average dust mass of these young disks at each radius bin, we obtain the initial solid mass profile (see Fig. 8): [7]

$$M_{\rm solids}(R_{\rm disk}) \approx 54 M_\oplus \left(\frac{R_{\rm disk}}{1\,{\rm AU}}\right)^{0.49} . \qquad (25)$$

By integrating the radial drift velocity in equation (9), we obtain the initial location from which dust grains are

[7] We exclude the first bin since typical ALMA rings are located at orbital distances distances beyond 10-20 AU.

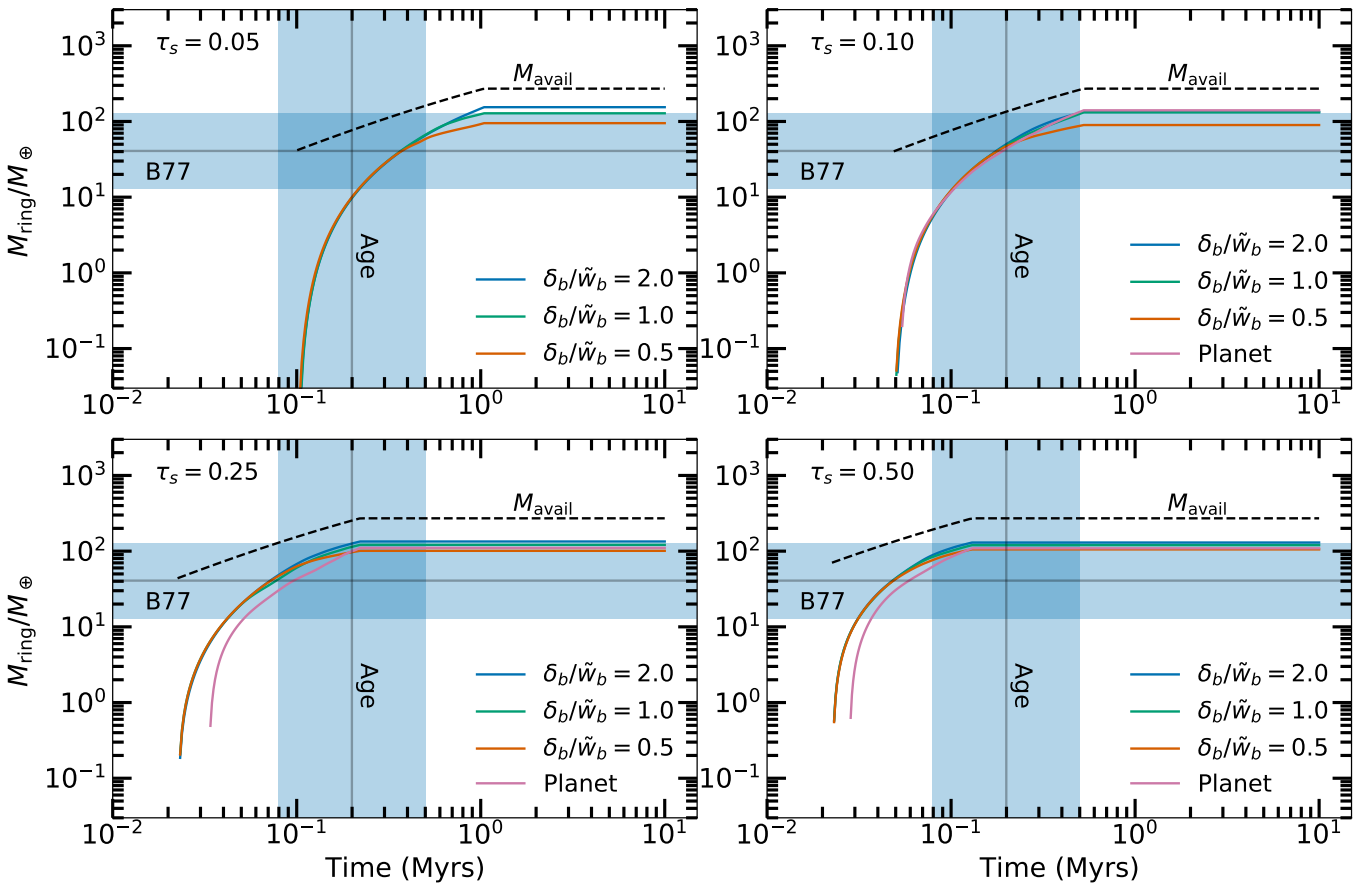

Figure 9. Dust mass inside a ring as a function of time (equation 28) for different particle Stokes number τ_s, mode of ring creation (Gaussian forcing vs. planet), and the profile of Gaussian forcing ($\delta_b/\tilde{w}_b$). The total amount of solid mass that would have drifted into the ring is annotated with $M_{\rm avail}$ (see equation 27). The inferred mass of the ring B77 (Dullemond et al. 2018) and the age of the host system Elias 24 (Andrews et al. 2018) are represented by the horizontal and vertical lines, respectively, with their 1-σ error illustrated with blue bars.

sourced

$$R_0(t) = R_{\rm f}\left[1 + 3\Pi\left(\frac{\tau_s}{1+\tau_s^2}\right)\Omega(R_{\rm f})\left(\frac{H}{R_{\rm f}}\right)t\right]^{2/3}, \tag{26}$$

where $R_{\rm f}$ is the orbital distance of the dust after drift in over a time t. For a dust ring located at $R_{\rm f}$, we use equation (25) to compute the total dust mass that drifts into $R_{\rm f}$ at any given time:

$$M_{\rm avail}(R_0(t)) \approx 54 M_\oplus\left[\left(\frac{R_0(t)}{1\,{\rm AU}}\right)^{0.49} - \left(\frac{R_{\rm f}}{1\,{\rm AU}}\right)^{0.49}\right]. \tag{27}$$

We can then express the total dust dust mass in the ring at time t as

$$M_{\rm ring}(t) = \int_{t_0}^{t} \epsilon_{\rm trap}(t')\left(\frac{dM_{\rm avail}(t')}{dt'}\right)dt', \tag{28}$$

where t_0 is the time at which we identify a dust ring for each simulation. We stop the integration at time t when $R_o(t) = 200$ AU, taken as the maximum size of a solid disk.

For a quantitative comparison with real data, we use the properties of the ring B77 in Elias 24 for its "median" properties (Dullemond et al. 2018). The total mass of the ring is $\approx 40.8\,M_\oplus$, and it is located at $R_f = 76.7$ AU from a star of mass $M_\star = 0.78\,M_\odot$. Figure 9 demonstrates that all the dust rings in our simulations are able to collect enough mass fast enough to match the inferred mass of B77 and the age of its host system Elias 24 within 1-σ uncertainty.[8] The maximum ring mass is reached earlier at larger τ_s since larger grains undergo more rapid drift.

5.1. *Dust rings: Gaussian forcing vs. planet-driven*

[8] We do not show $\tau_s = 0.05$ case with planetary forcing since its dust ring is transient.

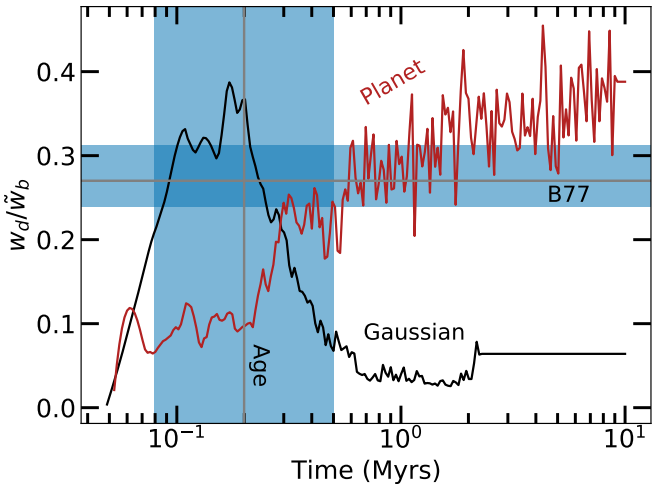

Figure 10. Time evolution of dust ring width in units of the width of the gas pressure bump (set to one H in all cases) for $\tau_s = 0.10$. The horizontal and vertical blue bars represent 1-σ uncertainty in the ratio of dust-to-gas pressure bump width (Dullemond et al. 2018, see their Figure 5 and Table 3) and in the estimated age of the host system Elias 24 (Andrews et al. 2018), respectively. Under Gaussian forcing (shown here only for $\delta_b/\tilde{w}_b = 1.0$), the particles concentrate more over time whereas under planet's tidal forcing, the particle ring puffs up over time.

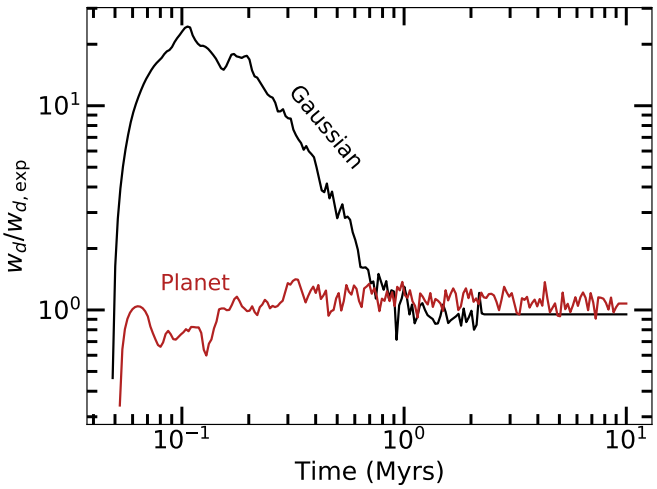

Figure 11. The ratio between the measured dust ring width and the expected width under drift-diffusion steady state (equation 33) for $\tau_s = 0.10$. The dust ring driven by planet's tidal forcing is described well by the balance between the radial drift and turbulent diffusion. In Gaussian forcing on the other hand (shown here only for $\delta_b/\tilde{w}_b = 1.0$), we see that the dust ring does not appear to reach a steady state until near the end of the simulation.

To identify differences between Gaussian-forced and planet-driven rings, we consider the degree of dust concentration measured as the ratio of the dust ring width (from our Gaussian fit to the dust radial distribution) to the gas pressure bump width (see Figure 10). In general, dust rings by Gaussian-forcing start puffy and sharpen with time whereas planet-driven rings gradually widen. We first discuss the behavior of planet-driven rings.

Assuming the dust rings are established by the drift-diffusion steady state:

$$\Sigma_{\mathrm{solid}} v_x = D_{d,\mathrm{ring}} d_r \Sigma_{\mathrm{solid}} \tag{29}$$

where

$$D_{d,\mathrm{ring}} \sim v_{\mathrm{rms}}^2 \frac{\tau_s}{\Omega} \tag{30}$$

is the diffusion coefficient of particles inside the ring (Youdin & Lithwick 2007), and

$$v_{\mathrm{rms}} = \sqrt{\frac{1}{N}\sum_j^N \left(v_{j,x} - \langle v_x \rangle\right)^2 + \left(v_{j,y} - \langle v_y \rangle\right)^2}, \tag{31}$$

is the root-mean-squared dispersion velocity of all particles within the dust ring, defined as $\pm 2\sigma$ from the centre of the Gaussian fit. Here, j and N denote the jth-particle and the total number of dust particles in the dust ring, respectively, and $\langle\rangle$ is the average of the N particles in the clump.

While we directly compute v_{rms} numerically, we can express it in terms of gas sound speed:

$$v_{\mathrm{rms}} = c_s \sqrt{\frac{\alpha_{\mathrm{eff}}}{1+\tau_s}} \tag{32}$$

where α_{eff} is the effective turbulence parameter. We stress that this α_{eff} is limited to 'turbulence' within the radial-azimuthal plane and is distinct from the degree of vertical turbulence. For all our simulations, v_{rms} rises with time. In planet-driven rings, $\alpha_{\mathrm{eff}} \sim 0.01$–$0.1$ whereas in Gaussian-forced rings, $\alpha_{\mathrm{eff}} \sim 10^{-4}$–$10^{-2}$.

If the center of the dust ring is located at the center of the gas pressure bump (in Gaussian form), then Σ_{solid} can be expressed as a Gaussian with a width

$$w_{d,\mathrm{exp}} \sim w_b \frac{v_{\mathrm{rms}}}{c_s}\sqrt{(1+\tau^2)} \sim w_b \sqrt{\frac{\alpha_{\mathrm{eff}}}{1+\tau}} \tag{33}$$

in the limit of $\tau_s < 1$ with v_{rms} expressed as equation 32 and w_b representing the width of the gas pressure bump. We then expect the dust to thicken with time as v_{rms} rises. Figure 11 demonstrates that the measured width of our dust ring under tidal forcing by a planet tracks well the expected ring width from drift-diffusion steady state.

On the other hand, dust rings under Gaussian forcing shows a systematic sharpening with time and only at the end of our simulation runs do we see that the width of the dust ring reaches an expected value (see Figure 11).[9] The decrease in the width of the ring makes sense from the perspective of snow ploughing effect. In the absence of strong diffusion, aerodynamic radial drift simply transports particles into a site of traffic jam. In general, particle rms velocities under Gaussian forcing are significantly smaller than that under planetary forcing and so it takes longer for the dust ring to reach a drift-diffusion steady state.

From Figure 10, we infer that both Gaussian and planetary forcing can reproduce the width of the B77 ring within the age of Elias 24. Past ∼0.3 Myrs, however, Gaussian forcing tends to create dust rings that are more concentrated (i.e., w_d/w_b is smaller) falling below ∼0.1. None of the rings studied in Dullemond et al. (2018), many of which are older than Elias 24, reach such tight w_d/w_b as we see in our Gaussian runs. We conclude that the rings observed in the DSHARP survey (Andrews et al. 2018) are more likely to be created by planetary perturbers or by other mechanisms that can scatter particles to similarly high random velocities.

We note that our Gaussian forcing is a simple parametrization of gas perturbations rather than a direct simulation of particular physical processes. Such 'smooth' Gaussian forcing may arise from condensation fronts, although the latent heat of condensation could drive hurricane-like vortices that can stir up particles to larger $v_{\rm rms}$ (e.g., Gerbig & Laughlin 2022). Magnetically-driven zonal winds can also create bands of gas perturbations and simulations report particles inside these zonal flows tend to have low $v_{\rm rms}/c_s \sim 0.01$–$0.02$ (see, e.g., Dittrich et al. 2013, their Figure 7), which is more akin to what we find in our simple Gaussian forcing runs.

5.2. *Gravitational collapse of dust inside the trap*

While we do not explicitly simulate the effect of self-gravity of the dust particles in our calculations, we can estimate the mass of clumps in the dust-rich bands that are expected to collapse into planetesimals or planetary bodies. We use the virial parameter for a spherical clump (e.g., Bertoldi & McKee 1992) to determine the size and mass of the bound clump in our simulations:

$$\alpha_{\rm vir} \sim \frac{5 v_{\rm rms,cl}^2 R_{\rm cl}}{G M_{\rm cl}} \leq 1, \tag{34}$$

where $v_{\rm rms,cl}$ is the root mean squared dispersion velocity of the dust particles in the clump, $R_{\rm cl}$ is the clump's radius, and $M_{\rm cl}$ is the total mass of dust in the clump. If $\alpha_{\rm vir} > 1$, dust particles have enough kinetic energy to expand and move through the gas, whereas dust clumps with $\alpha_{\rm vir} \leq 1$ are gravitationally bound. We note that this collapse condition is equivalent (within a numerical factor) to the diffusion-limited collapse criterion for planetesimals outlined by Klahr et al. (2018) and Gerbig et al. (2020) which derives from the condition where the contraction timescale

$$t_{\rm contr} = \frac{\Omega}{4\pi G \rho_{\rm cl} \tau_s} \tag{35}$$

(where $\rho_{\rm cl} = 3M_{\rm cl}/4\pi R_{\rm cl}^3$ is the density of the clump) is shorter than the diffusion timescale

$$t_{\rm diff} = \frac{R_{\rm cl}^2}{D_d} \tag{36}$$

with

$$D_d \sim v_{\rm rms,cl}^2 \frac{\tau_s}{\Omega} \tag{37}$$

the particle diffusion coefficient (Youdin & Lithwick 2007). The collapse criterion $t_{\rm contr} < t_{\rm diff}$ boils down to

$$\frac{v_{\rm rms,cl}^2 R_{\rm cl}}{3 G M_{\rm cl}} \sim \alpha_{\rm vir}/15 < 1. \tag{38}$$

By defining a bound clump as those with $\alpha_{\rm vir} < 1$, our dust clumps are guaranteed to collapse against turbulent diffusion.

We identify a bound clump for all our simulations as follows:

1. We obtain the (x,y)-coordinate of the densest point within the dust ring, defined as a radial strip of total width 4σ centered at the peak of the Gaussian fit. Before identifying the densest point, we smooth the 2-dimensional distribution of dust grains using a Gaussian kernel density estimator (KDE).[10] This (x,y)-coordinate locates the center of our clump.

2. We first set $R_{\rm cl} = H_{\rm solid}$, where, following Youdin & Lithwick (2007), we define $H_{\rm solid}$ as the dust scale height

$$H_{\rm solid} = H \sqrt{\frac{\alpha}{\alpha + \tau_s}} \tag{39}$$

[9] The initial rise in w_d at $\lesssim$0.1 Myrs is due to our fitting routine forcing a Gaussian at the edge of the dust drift front that has not yet collected into a visible local peak in dust concentration.

[10] The smoothness of the KDE is set by the bandwidth parameter, which for the present work is given by the "Scott's Rule"(i.e., $N^{-1/(d+4)}$, where N is the number of data points and d the number of dimensions, see, e.g., Scott 2015).

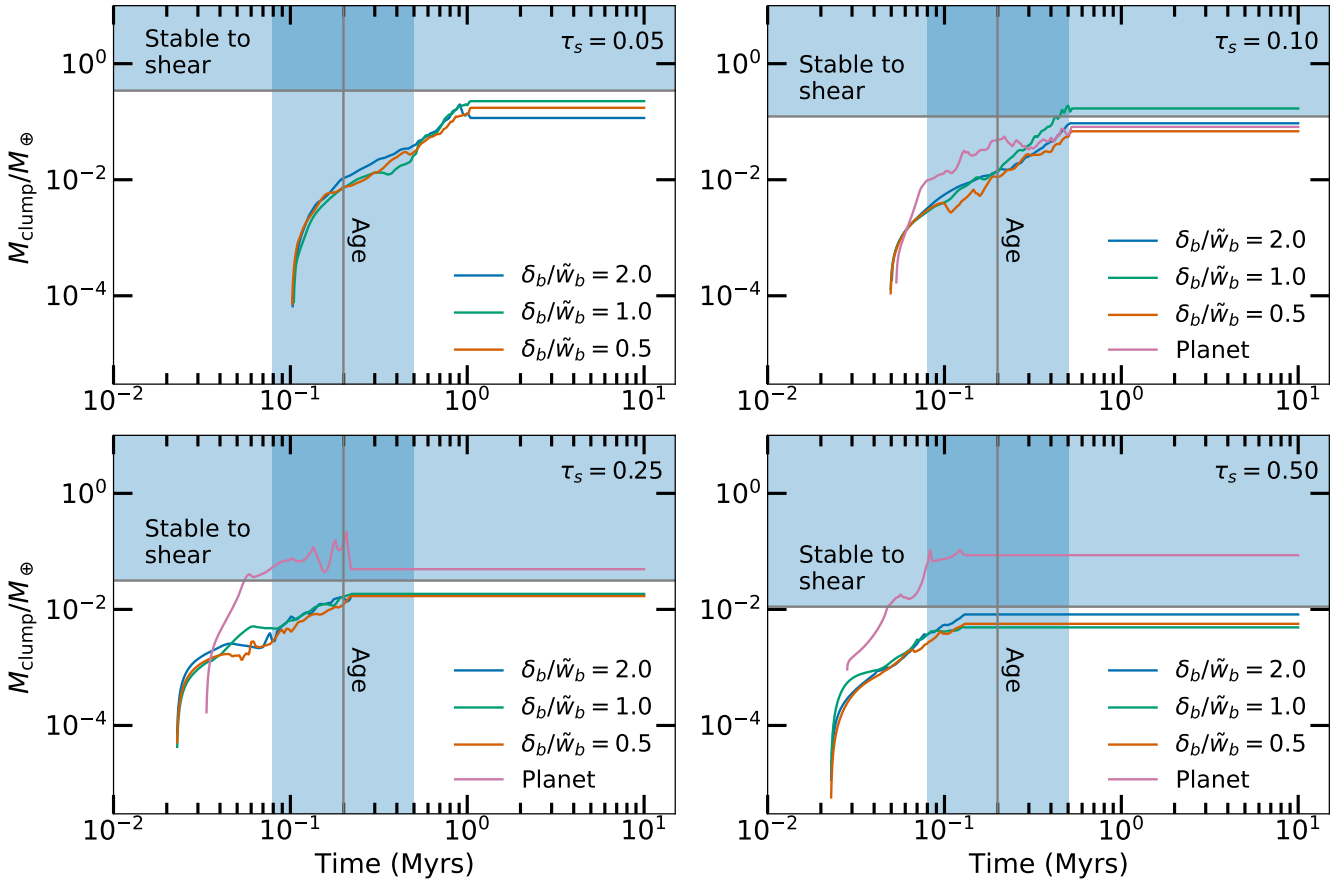

Figure 12. Mass evolution of the bound dust clump in the dust-rich bands; annotations are identical to that of Figure 9, with the addition of a grey horizontal line delineating the minimum mass for stability against tidal shear. In most of our simulation runs, we expect that the dust clumps, if at their maximal size, would be sheared apart.

with Shakura-Sunyaev parameter $\alpha = 10^{-3}$ as this is the maximum expected value from the geometry of ringed disks (Pinte et al. 2016) and from CO line measurements in protoplanetary disks (e.g., Flaherty et al. 2017). We note that this α probes the vertical turbulence and is distinct from $\alpha_{\rm eff}$ previously defined.

3. Within a radius of $R_{\rm cl}$ centered at the densest point, we calculate the $v_{\rm rms,cl}$ of dust particles using equation 31.

4. The mass of the clump is calculated as $M_{\rm cl} = \pi R_{\rm cl}^2 \Sigma_{\rm solid}$, where $\Sigma_{\rm solid}$ is the solid surface density of the dust ring. To estimate $\Sigma_{\rm solid}$ as a function of time, we integrate the Gaussian fit of the dust ring within 2σ, and normalize it to the mass of the ring as computed in equation 28:

$$\Sigma_{\rm solid} \sim \frac{M_{\rm ring}}{2\pi C}\,, \tag{40}$$

where

$$C = \int_{R_f-2\sigma}^{R_f+2\sigma} e^{-0.5(x-R_f)^2/\sigma^2}\, x\, dx\,. \tag{41}$$

The normalization C is close to and slightly larger than $2R_f\sigma$. We note that in all our simulation snapshots (except at the very earliest times), the x-coordinate of the center of the clump is close enough to the radial center of the dust ring so that we do not need to worry about the Gaussian fall-off in $\Sigma_{\rm solid}$.

5. If the clump's virial parameter at $R_{\rm cl} = H_{\rm solid}$ is larger than 1, we iteratively shrink $R_{\rm cl}$ and follow steps 3 and 4 above until we reach $\alpha_{\rm vir} \leq 1$. We find that step 5 is never invoked in any of our simulation snapshots (i.e., all our "bound" clumps are at the maximum size).

In protoplanetary disks, clumps that can gravitationally collapse against turbulent diffusion may still be sheared apart. To be stable against tidal shear, the

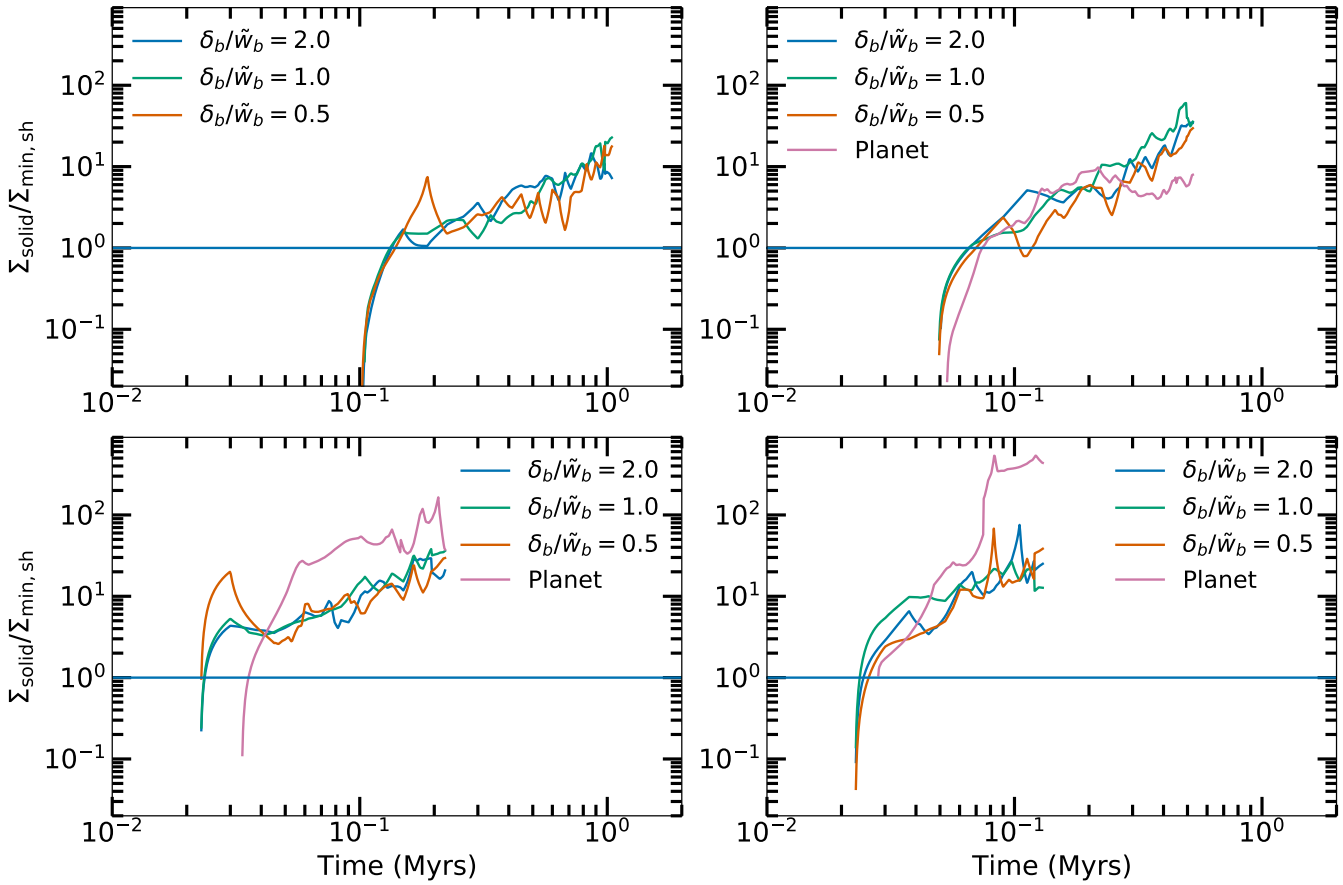

Figure 13. The ratio of solid density in the dust ring to the minimum density required to for a clump to be bound against turbulent diffusion and be stable against tidal shear (see equation 46). Values are shown until the solids out to maximum disk radius 200 AU drift into $R_f = 76.7$ AU. Except for the initial fraction of evolution, all dust rings are dense enough to nucleate smallest stable planetesimals.

clump's self-gravity must be larger than tidal acceleration (Gerbig et al. 2020):

$$\frac{GM_{\rm cl}}{R_{\rm cl}^2} > 3\frac{GM_\star}{R_f^2}\left(\frac{R_{\rm cl}}{R_f}\right). \tag{42}$$

We find that $R_{\rm clump} = H_{\rm solid}$ always to keep the clump's $\alpha_{\rm vir} \leq 1$ and so setting the clump radius as the dust scale height, the condition for stability against shear:

$$M_{\rm cl} > 3M_\star\left(\frac{H}{R_f}\right)^3\left(\frac{\alpha}{\alpha+\tau}\right)^{3/2}. \tag{43}$$

As illustrated in Figure 12, our dust rings, scaled to the properties of B77 in Elias 24, are unable to nucleate stable bound clumps at their maximal size except for three distinct simulation setups: Gaussian-forcing ($\delta_b/\tilde{w}_b = 1$) with $\tau_s = 0.10$ and planet-forcing with $\tau_s = 0.25, 0.50$.

The difficulty in creating stable planetesimal/planetary bodies stems from two effects. At small τ_s, the minimum clump mass to be stable against shear is larger because of larger H_d (i.e., clumps are more extended). Dust rings need to collect more mass to reach the stability limit but this collection takes a while since the radial drift is slower at smaller τ_s. In the specific case of B77, the observed ring is located at a sufficiently wide orbit that we run out of dust mass before the clumps can grow large enough to be stable against shear. We note that creating a stable clump within the age of the system becomes easier even at small τ_s if the dust ring is located closer to the star and the system is older.

At large τ_s, the minimum clump mass for shear-stability is smaller because of smaller H_d (i.e., clumps are more compact) and so dust rings do not need to collect as much mass. However, for Gaussian-forced runs, the dust rings are puffy in the first ~1 Myr and so $\Sigma_{\rm solid}$ is small. Combined with smaller $R_{\rm cl}$ at large τ_s, $M_{\rm cl}$ is also small. Again, in the specific case of B77 which is at a wide orbit, the disk runs out of material before the dust ring can sharpen. Placing the dust ring at closer-in

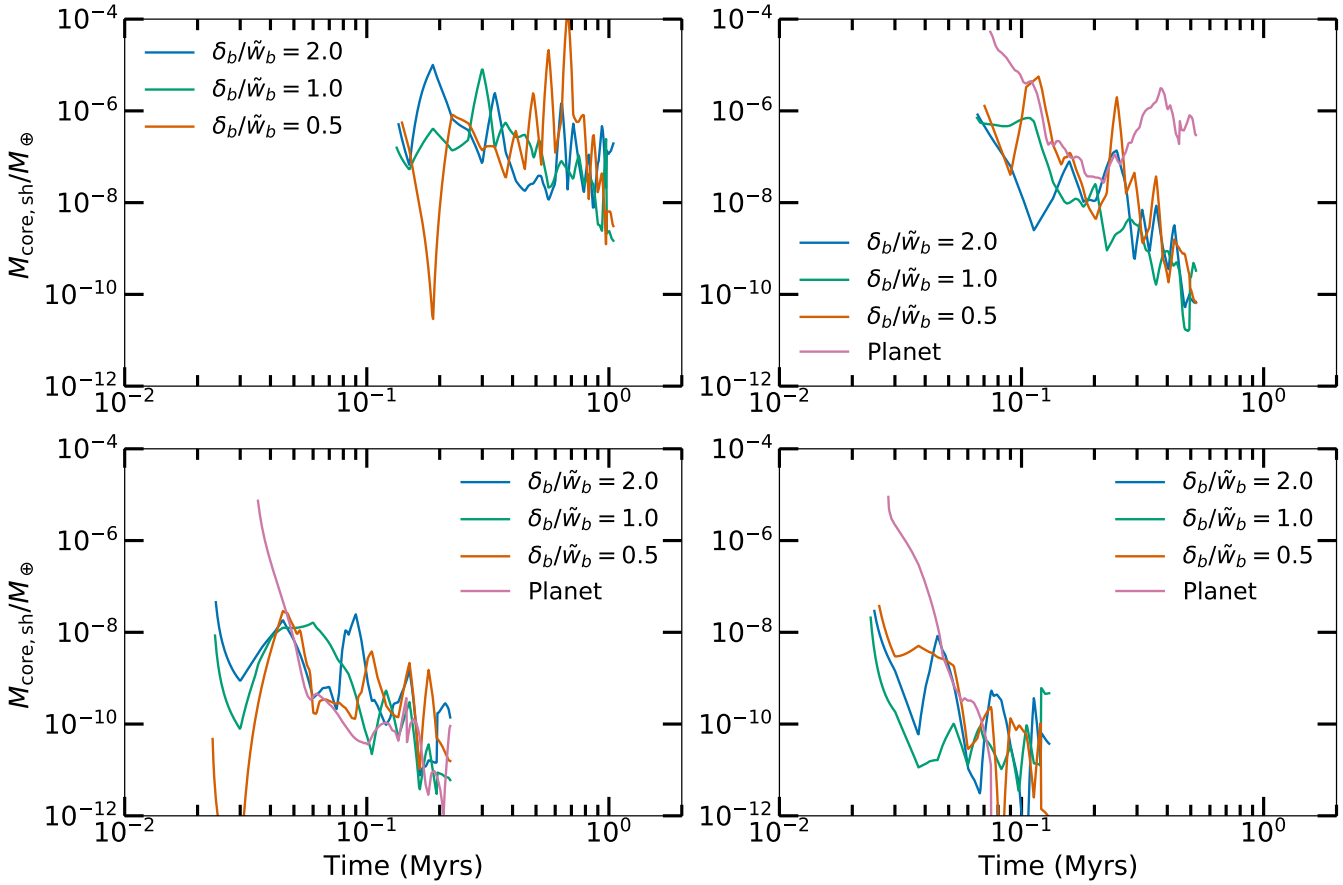

Figure 14. Masses of smallest possible bound clumps stable against tidal shear. Values are shown from when $\Sigma_{\rm solid} \geq \Sigma_{\rm min,sh}$ and until the solids out to maximum disk radius 200 AU drift into $R_f = 76.7$ AU.

orbits would render easier the formation of stable bound clumps.

For $\tau_s = 0.25$ and 0.50, planet-driven rings can easily nucleate stable dust clumps. Since planet-driven rings are narrower at earlier times as compared to Gaussian-forced rings (see Figure 10), $\Sigma_{\rm solid}$ is larger and these rings are able to create more massive clumps. In general, the steady state width of the dust rings is narrower for larger τ_s (see equation 33), and the minimum mass for shear stability is also lower because $H_{\rm solid}$ is smaller.

It is possible that we could define a smaller dust clump $R_{\rm cl} < H_{\rm solid}$ so that it is shear-stable within the age of Elias 24. Consider $R_{\rm cl} = f_R H_{\rm solid}$ where $f_R \leq 1$ is a numerical factor. The collapse criterion against turbulent diffusion (equation 38) sets the lower limit on f_R:

$$f_R > \frac{v^2_{\rm rms,cl}}{3\pi G \Sigma_{\rm solid} H_{\rm solid}}, \tag{44}$$

where we used $M_{\rm cl} = \pi \Sigma_{\rm solid} R^2_{\rm cl}$. In order for this clump to be stable against tidal shear,

$$\frac{v^2_{\rm rms,cl}}{3\pi G \Sigma_{\rm solid}} < (R_{\rm cl} = f_R H_{\rm solid}) < \frac{\pi \Sigma R^3_f}{3 M_\star}. \tag{45}$$

It follows that this condition will be met if

$$\Sigma^2_{\rm solid} > \frac{M_\star v^2_{\rm rms,cl}}{\pi^2 G R^2_f} = \Sigma^2_{\rm min,sh}. \tag{46}$$

As demonstrated in Figure 13, for the majority of the evolution, our dust rings meet the density criterion for the creation of the smallest planetesimal stable against tidal shear. The corresponding masses of such clumps are shown in Figure 14, which are smaller than Ceres $\sim 10^{-4} M_\oplus$. We conclude that while it is unlikely to create large planetesimals out to the size of the dust scale height in the dust rings we simulate, it is possible to create smaller bodies down to sub-Ceres masses.

6. PLANET FORMATION IN DUST RINGS

Either a Gaussian forcing or tidal forcing by a planet creates a long-lasting pressure bump that can collect particles into an axisymmetric or nearly axisymmetric ring. Scaled to the properties of B77 in Elias 24 (Andrews et al. 2018), we find that all of our rings are able to collect enough dust grains to match the measured mass (Dullemond et al. 2018). In addition, all our dust rings

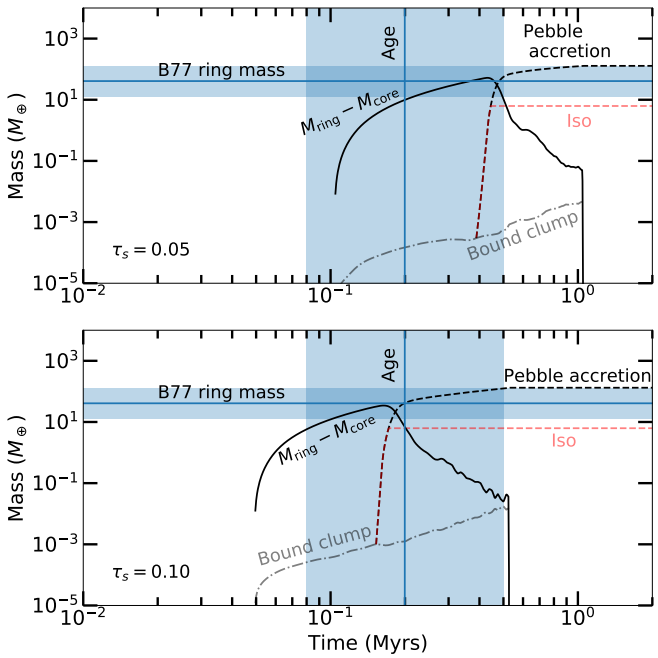

Figure 15. Mass growth of a bound clump under pebble accretion within a dust ring for a Gaussian bump ($\delta_b/\tilde{w}_b = 1$). Accretion begins when the bound clump reaches $M_{\rm settl}$ and conditions for shear-stability are met (equations 52 and 53). For our simulation parameters, the pebble isolation mass (annotated here as 'Iso') is $\sim 6.25 M_\oplus$ as computed using the scaling relationship of Bitsch et al. (2018). The vertical and horizontal lines delineate the inferred ages and ring masses of B77 in Elias 24 with the blue bars illustrating 1-σ uncertainty (Andrews et al. 2018; Dullemond et al. 2018).

are expected to nucleate small, bound and shear-stable clumps. In this section, we investigate the expected mass growth of these clumps via pebble accretion.

In general, the mass growth rate of a core embedded in a disk of solids is

$$\dot{M}_{\rm core} = 2\Sigma_{\rm solid} R_{\rm acc} v_{\rm acc} \times \min(1, R_{\rm acc}/H_{\rm solid}) \quad (47)$$

where particles that enter within a radius $R_{\rm acc}$ of the core at speeds of $v_{\rm acc}$ will be accreted to the core. Growth by pebble accretion begins in earnest when $\tau < 1$ and when the particle stopping time is shorter than its interaction time with the core (i.e., the "settling" regime as identified by Ormel & Klahr (2010); see also review by Ormel (2017)):

$$\tau_s/\Omega < R_{\rm acc}/V_{\rm acc}. \quad (48)$$

We first establish the bound clump mass at which accretion is in this settling regime. Following the procedure of Lin et al. (2018), we compute $R_{\rm acc}$ and $v_{\rm acc}$ in the settling regime and verify that equation 48 is satisfied. For all our simulations, $\tau_s < 1$ so we use

$$v_{\rm acc} = \sqrt{\left(v_{\rm hw} + \frac{3}{2}\Omega R_{\rm acc}\right)^2 + v_{\rm rms}^2} \quad (49)$$

where $v_{\rm hw} = -(c_s^2/2\Omega a)(\partial \log P/\partial \log a)$ is the headwind velocity evaluated at the location of the bound clump (i.e., the radial center of the dust ring), c_s the sound speed, a the orbital distance, and P the gas pressure. Under the settling condition (equation 48), particles that accrete onto the core attain a terminal velocity during the encounter so that

$$\frac{v_{\rm acc}}{4} = \frac{GM_{\rm core}}{R_{\rm acc}^2}\frac{\tau_s}{\Omega} \quad (50)$$

where G is the gravitational constant. From this, $R_{\rm acc}$ is solved for by finding the root of

$$\frac{9}{4}b^6 + 3\zeta b^5 + \left(\zeta^2 + \zeta_{\rm rms}^2\right) b^4 - 144\tau_s^2 = 0 \quad (51)$$

where $b \equiv R_{\rm acc}/R_{\rm Hill}$, $R_{\rm Hill} = \mu_M^{1/3} a$, $\mu_M \equiv M_{\rm core}/3M_\star$, $\zeta \equiv v_{\rm hw}/v_{\rm Hill}$, $v_{\rm Hill} = \Omega R_{\rm Hill}$, and $\zeta_{\rm rms} \equiv v_{\rm rms}/v_{\rm Hill}$. We find that dust clumps need to be at least 0.0003, 0.001, 0.03, and $0.1 M_\oplus$ for τ_s =0.05, 0.1, 0.25, 0.5, respectively, to be in the settling regime under Gaussian forcing. For planet-driven bumps, the minimum mass of the initial dust clump capable of undergoing pebble accretion (in the settling regime) is 0.03, 0.03, and $0.1 M_\oplus$ for τ_s =0.1, 0.25, and 0.5, respectively.

For these initial cores to be stable against tidal shear, the dust ring needs to be sufficiently dense. Labeling the minimum core mass for pebble accretion as $M_{\rm settl}$ and letting $M_{\rm settl} = \pi\Sigma_{\rm solid}(f_{R,{\rm settl}} H_{\rm solid})^2$, the shear-stability condition can be re-written as

$$\Sigma_{\rm solid} > \left(\frac{M_{\rm settl} M_\star^2}{\pi^3 R_f^6}\right)^{1/3}. \quad (52)$$

In addition,

$$\frac{M_{\rm settl}}{M_\star} < \left(\frac{H_{\rm solid}}{R_f}\right)^{1/3} \quad (53)$$

to ensure $f_{R,{\rm settl}} < 1$. We find that the above conditions are met only when $\tau_s = 0.05$ and 0.10 for Gaussian-forcing. For planet-driven bumps, the above conditions are met for all possible $\tau_s = 0.1, 0.25, 0.5$.

We find that as soon as pebble accretion begins, the clumps can immediately accrete the entire mass of the ring. Example growth tracks are illustrated in Figure 15 where we highlight the Gaussian-forced rings whose the planetary growth is relatively slow as compared to

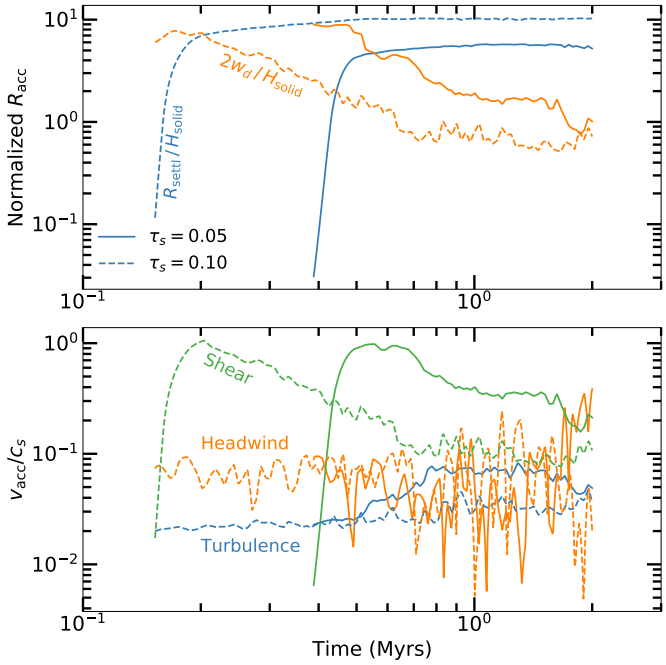

Figure 16. Top: accretion radius under the settling condition ($R_{\rm settl}$, evaluated by solving equation 51) and the width of the dust ring $2w_d$ with respect to $H_{\rm solid}$. Bottom: relative contribution of shear, headwind, and turbulent random velocities to the accretion velocity $v_{\rm acc}$, normalized by the sound speed, all evaluated for the Gaussian bump ($\delta_b/\tilde{w}_b = 1$). In the calculation of the shear velocity, the accretion is set to the minimum between $R_{\rm settl}$ and $2w_d$.

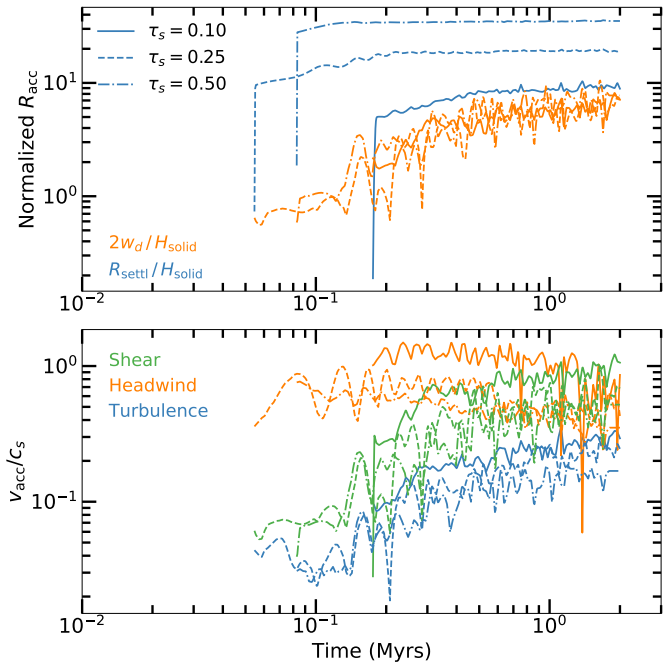

Figure 17. Likewise as Figure 16 but for planet-driven rings.

planet-driven rings. To understand these short accretion times, we provide analytic estimates of the timescales to ingest the entire content of the ring ($M_{\rm ring}/\dot{M}_{\rm core}$).

From Figures 16 and 17, we infer that the accretion is initially in the 3-dimensional regime ($R_{\rm acc} = \min(R_{\rm settl}, 2w_d) < H_{\rm solid}$). In this case, we obtain

$$\dot{M}_{\rm core} = \frac{8\Sigma_{\rm solid} G M_{\rm core} \tau_s}{c_s} \left(\frac{\alpha+\tau_s}{\alpha}\right)^{1/2} \tag{54}$$

by combining equations 47 and 50. The core mass grows exponentially in time with the mass doubling time ($M_{\rm core}/\dot{M}_{\rm core}$) being independent of the core mass. As shown in the third panel from the top of Figure 18, our mass doubling timescales are extremely short as compared to the age of Elias 24, which explains the rapid climb in $M_{\rm core}$ seen in Figure 15.

The transition to the 2-dimensional regime ($R_{\rm acc} > H_{\rm solid}$) is almost immediate in all the runs except for the planet-driven ring of $\tau_s = 0.25$ whose accretion stays in the 3D regime for at least 0.1 Myrs. In the 2D accretion, the growth rate depends on the exact behavior of $R_{\rm acc}$ and $v_{\rm acc}$. We see from Figure 16 that $R_{\rm acc} \sim R_{\rm settl}$ for the initial ∼0.1 Myr of 2D accretion in Gaussian-forced rings. During this time, $v_{\rm acc}$ is dominated by the shear velocity so that $v_{\rm acc} \sim (3/2)\Omega R_{\rm settl}$. The corresponding accretion rate is

$$\begin{aligned}\dot{M}_{\rm core} &= 3\left(\frac{8}{3}\right)^{2/3} \Sigma_{\rm solid} a^2 \Omega \tau_s^{2/3} \left(\frac{M_{\rm core}}{M_\star}\right)^{2/3} \\ &= \frac{3}{2}\left(\frac{8}{3}\right)^{2/3} M_{\rm ring} \frac{\Omega}{2\pi} \left(\frac{a}{w_d}\right) \tau_s^{2/3} \left(\frac{M_{\rm core}}{M_\star}\right)^{2/3}\end{aligned} \tag{55}$$

where we used $\Sigma_{\rm solid} = M_{\rm ring}/4\pi a w_d$. The orbital time at 76.7 AU around 0.78 $M_\odot$ star is ∼760 years. Since $w_d \sim 0.3$ and $H/a = 0.05$ in our simulation setup, $w_d/a = 0.015$. For $\tau_s = 0.1$, $M_{\rm core}$ at the transition from 3D to 2D accretion is $\sim 0.17 M_\oplus$. It follows that the time to ingest the entire dust ring $M_{\rm ring}/\dot{M}_{\rm core} \sim 760\,{\rm yrs} \times (3/8)^{2/3}/(3/2)/0.015/0.05^{2/3}/(0.17 M_\oplus/M_\star)^{2/3} \sim 0.4$ Myrs. For $\tau_s = 0.05$, $w_d \sim 0.6$ and $M_{\rm core}$ at transition $\sim 0.7 M_\oplus$ and a similar analysis provides $M_{\rm ring}/\dot{M}_{\rm core} \sim 0.3$ Myrs, which we verify in the bottom panel of Figure 18.

From Figure 17, we infer that the accretion radius of a clump in planet-driven rings will be limited by the width of the dust ring once the accretion enters the 2D regime ($R_{\rm acc} = 2w_d$) and that the accretion velocity is dominated by the local headwind at all times. The accretion rate is then

$$\dot{M}_{\rm core} = 4 M_{\rm ring} \frac{\Omega}{2\pi} \left(\frac{v_{\rm hw}}{a\Omega}\right). \tag{56}$$

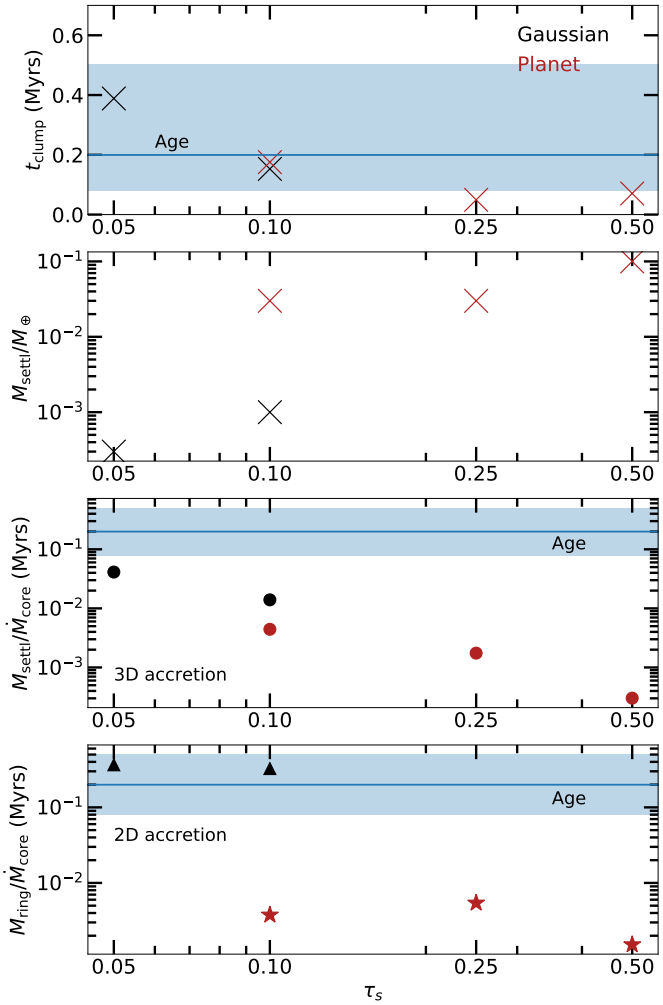

Figure 18. Top: the time at which pebble accretion begins. Second from the top: the initial clump mass for pebble accretion (i.e., minimum mass required for settling accretion). Third from the top: core mass doubling time in 3D accretion ($R_{\rm acc} < H_{\rm solid}$; see equation 54). Bottom: time to ingest the entire dust ring in 2D accretion ($R_{\rm acc} = 2w_d > H_{\rm solid}$). Triangles correspond to shear-dominated accretion relevant for Gaussian-forced rings (equation 55) whereas stars represent headwind-dominated accretion relevant for planet-driven rings (equation 56). For all panels, black and red markers denote Gaussian vs. planet-forced rings, respectively. The horizontal line and the blue bar illustrates the age of Elias 24 and its 1-σ error, respectively.

From Figure 17, we infer $v_{\rm hw} \sim 0.4$–$1c_s$ and since $H/a = 0.05$, $v_{\rm hw}/a\Omega \sim 0.02$–$0.05$. Equation 56 implies the core is able to accrete the entire ring mass over just 760 years / 4 / 0.05 $\sim 4 \times 10^3$–10^4 years, as shown in the bottommost panel of Figure 18.

For all the rings we simulate that are capable of creating a stable clump massive enough for pebble accretion, the mass growth of the core is rapid, so much so that we expect the entire ring to be engulfed by the core within the age of the system $\lesssim$1 Myr. Our result differs from that of Morbidelli (2020) who report that planets can only grow at best (defined by them as when the pebble-accreting planetary object is at the radial center of the dust ring) up to $\sim 1 M_\oplus$ in rings such as B77 in Elias 24. One minor difference is our higher $\Sigma_{\rm solid}$, stemming from our tight ring width w_d, which accelerates the initial mass doubling in the 3D regime. More crucially, we adopt a larger τ_s (mainly for the cost of numerical simulation): our smallest $\tau_s = 0.05$ as compared to Morbidelli (2020) who used $\tau_s = 10^{-3}$ and pebble accretion is expected to be slow for smaller τ_s.

In 3D pebble accretion, $\dot{M}_{\rm core} \propto \tau_s^{3/2}$ for $\tau_s \ll \alpha$ and we see the expected overall increase in the mass doubling timescale with smaller τ_s in this regime in Figure 18. Once the accretion enters the 2D phase, the trend with τ_s is less obvious. For Gaussian-forced rings ($R_{\rm acc} \sim R_{\rm settl}$, shear-dominated), even though $\dot{M}_{\rm core} \propto \tau_s^{2/3}$ in this regime, $M_{\rm core}$ at the 2D to 3D transition is larger at smaller τ_s and the two effects can cancel each other out. For example, we see little difference between the ring ingestion timescale of Gaussian-forced rings at $\tau_s = 0.05$ and 0.10. For planet-driven rings ($R_{\rm acc} = 2w_d$, headwind-dominated), $M_{\rm ring}/\dot{M}_{\rm core}$ is independent of τ_s. The core mass doubling time ($M_{\rm core}/\dot{M}_{\rm core}$) however would be τ_s-dependent since at a given time, $M_{\rm ring}$ would be smaller at lower τ_s due to slower radial drift. As far as we can tell, the accretion regime used by Morbidelli (2020) is 2D, local-headwind dominated regime under the assumption of absolute maximum possible accretion (i.e., the entire dust front undergoing radial drift has the potential to be accreted onto the core, not just the ones that enter $R_{\rm acc}$).

We conclude that the dust rings of characteristics similar to that of DSHARP dataset are, under some circumstances, capable of creating planetary mass objects and if so, these objects would engulf the entire dust within the ring almost instantly. We note that before the ingestion of the entire dust ring, it is likely that these clumps would reach the isolation mass and perturb the ring, perhaps creating another dust ring external to its orbit. For our simulation setup, the expected pebble isolation mass is only $\sim 6.25 M_\oplus$ using the scaling relationship of Bitsch et al. (2018) with $\alpha = 10^{-3}$, smaller than the total ring mass $\gtrsim 10 M_\oplus$. By definition, however, pebble isolation masses would perturb the surrounding gas (and therefore the dust ring in which the core resides) potentially creating a secondary ring in the outer orbit.

The fact that we see these rings over $\sim$1 Myr suggests that such rapid planet formation likely does not

happen. It may be that the dust particles that make up the rings have particularly small τ_s whose relevant dynamical timescales (e.g., the drift time to fill up the ring and the time of clump formation) are longer. We find however that when $\tau_s = 0.05$, planet-driven dust rings tend to be transient as particles are coupled to the advective flow of gas onto the planet, although such transiency may be a feature of our local shearing box approximation. Alternatively, the measured dust rings may be driven by non-planetary mechanisms that can establish a Gaussian pressure bump and scatter particles to sufficiently high $v_{\rm rms}$ to reproduce the correct ring width. Such a scenario could accommodate both low τ_s (although it cannot be so small that it takes too long to collect enough dust mass within a ring) and a high $\tau_s > 0.1$ where the disk runs out of material due to fast radial drift before creating a bound, stable clump massive enough to trigger pebble accretion.[11]

As we mentioned previously, the nucleation of dust clumps stable to tidal shear is easier at shorter orbital distances. If typical protoplanetary disks are constantly creating dust rings over a wide range of stellocentric distances and quickly coagulate into planetary objects that create secondary rings, we would expect to see older systems to harbor rings at wider orbits. Such trend however is likely complicated by the intrinsic variance in the size of the protoplanetary disks; in fact, we see no obvious sign of such trend in the DSHARP survey.

We close this section with a comment on the possibility of creating multiple clumps in a single ring. In 3D accretion, all initial clumps would be subject to the same mass doubling time (i.e., $M_{\rm core}/\dot{M}_{\rm core} \propto M_{\rm core}^0$) and so the distribution of relative masses would stay the same. In 2D accretion, from equations 55 and 56, we infer that the mass doubling timescale of a core would lengthen for massive cores. If multiple clumps form in a given ring, the final masses would then approach similar values (Kretke & Levison 2014). As multiple planetary objects would be placed within a narrow range of orbital distances, their orbits would likely become unstable causing either mergers or ejecta (most likely ejecta at the large orbital distances of DSHARP rings).

7. SUMMARY AND CONCLUSIONS

[11] However, we add a caveat to this latter point as the main reason why we are unable to create massive clumps under Gaussian forcing at high τ_s is because of initially small $\Sigma_{\rm solid}$. If self-consistent accounting for a non-planetary physical mechanism can perturb particles to sufficiently high $v_{\rm rms}$, then we expect the dust ring to behave as would be expected from drift-diffusion and we would expect higher clump masses.

Using 2-dimensional (radial-azimuthal plane) shearing box simulations, we studied the interaction between an inward flux of dust particles and gas in a pressure bump, considering both a Gaussian-forced bump (as may arise from condensation fronts or magnetically-driven zonal flows) and planet-driven perturbations. Unlike previous studies, we constantly supplied dust particles from the right edge of the simulation box to mimic the inward drift rather than starting with a uniform distribution of particles across the whole box. The main findings are the following:

1. Dust particles collect away from the center of the pressure bump for both Gaussian and planet-forcing (see Figures 2-3 and 6). Within the trap, dust particles distribute initially in non-axisymmetric structures and overtime, transform into more axisymmetric rings. Larger τ_s particles collect more readily into thinner rings.

2. While continuous forcing of the gas ensures the re-establishment of a pressure bump, the back-reaction of dust perturbs significantly the gas pressure profile especially when the local dust-to-gas ratio $\gtrsim$0.1 and enhances the degree of dust collection (see Figure 2).

3. The efficiency of the dust trap $\epsilon_{\rm trap}$ asymptotes to values between $\sim 40\% - 80\%$ for the runs using Gaussian forcing (see Figure 4). The initial leakage of particles causes a drop in $\epsilon_{\rm trap}$ to $\sim$0.2 between $\sim$1 and 4 drift times in all our simulations, and $\epsilon_{\rm trap}$ recovers afterwards; the degree of leaking is stronger for larger τ_s which are harder to capture against rapid radial drift. For the planet-induced bump, we find that gas vortices near the trap help to collect particles, maintaining $\epsilon_{\rm eff} \sim 0.6$–$0.8$ at all times for $\tau_s = 0.25$ and 0.5. For smaller τ_s, particles are advected out of the dust ring following the gas flows that are attracted to the planet, reducing the significantly the efficiency of the trap (down to 40% for particles of $\tau_s = 0.1$, and to $\approx 0\%$ for $\tau_s = 0.05$, see Fig. 7).

4. With the high $\epsilon_{\rm eff}$, our dust rings are able to collect enough mass within $\lesssim$1 Myr to explain the inferred masses of typical rings analyzed in the DSHARP survey (Andrews et al. 2018; Dullemond et al. 2018). See Figure 9.

5. Under Gaussian forcing, dust rings start puffy and sharpen with time, reminiscent to snow-ploughing effect. Under planet-forcing however, dust rings start narrow and widen with time, in accordance

with drift-diffusion steady state as grains are excited to larger velocity dispersion. The measured width of dust rings in DSHARP data are more similar to our planet-driven cases (see Figure 10).

6. At their maximal size set by the particle disk scale height (assuming $\alpha = 10^{-3}$), all our simulated rings are expected to nucleate dust clumps that are gravitationally bound against turbulent diffusion but in most cases are expected to be sheared apart (see Figure 12). Smaller planetesimals (e.g., smaller than Ceres) may still form.

7. In the subset of cases where bound and stable clumps massive enough to trigger pebble accretion nucleate, such clumps are expected to undergo rapid mass growth ingesting the entire dust content within the ring over timescales $\lesssim$1 Myr.

The fact that we see concentric dust rings in many of protoplanetary disks imaged with ALMA suggests that the formation of planetary bodies in these rings must be either a rare or a slow process, at least at the wide orbits that are accessible to current interferometric imaging technology. From our findings, we infer that the real-life disk rings are likely composed of particles of small $\tau_s \leq 0.05$ so as to delay the creation of dense dust rings, the nucleation of massive planetesimals, and therefore the onset of core growth. One issue with such a solution is that these small particles are not expected to remain in dust rings for long when they are perturbed by a planet, yet we found that the width of the observed dust rings are better matched by planet-driven rings. The transient nature of $\tau_s \leq 0.05$ rings we found with GIZMO needs to be verified with global disk simulations.

While we prescribed a continuous Gaussian forcing of a fixed form, the real-life non-planetary origin of gas pressure maxima will likely introduce more complexity, potentially scattering dust particles to higher random velocities and creating a dust ring that is as thick as what we observe in ALMA disks. Furthermore, we ignored the planet's gravity on dust particles in order to isolate the dust-gas dynamics. As verified in a subset of cases we simulated, turning on planet's gravity acting on dust could cause a stronger leak of particles, reducing the efficiency of the trap and rendering dust rings as transient substructures, particularly for particles of $\tau_s \leq 0.1$, which are already affected by gas inflows into the planet due to the strong coupling with the gas.

Given the difficulty in maintaining the dust ring against advection at low τ_s and against engulfment by a planetary object embedded within the ring at high τ_s, the origin of dust rings we see in protoplanetary disks may trace to non-planetary mechanisms. If these rings are the sites of planet formation, then we expect the inner rings to rapidly collapse into a planet or planets first, potentially creating another ring outside their orbits. Under this hypothesis, dust rings would appear at systematically wider orbits for older systems. A larger sample than what we currently have that spans a wider range of ages to search for a trend between the ring location and age may help distinguish between the different origin channels of dust rings.

We thank Jonathan Squires for helpful discussions and Ge Chen for providing preliminary analyses. E.J.L. gratefully acknowledges support by the Sherman Fairchild Fellowship at Caltech, by NSERC, by le Fonds de recherche du Québec – Nature et technologies (FRQNT), by McGill Space Institute, and by the William Dawson Scholarship from McGill University. J.R.F. acknowledges support by a Mitacs Research Training Award, a McGill Space Institute (MSI) Fellowship, and thanks the Department of Applied Mathematics at the University of Colorado Boulder, for hospitality. Support for PFH was provided by NSF Research Grants 1911233, 20009234, 2108318, NSF CAREER grant 1455342, NASA grants 80NSSC18K0562, HST-AR-15800. This research was enabled in part by support provided by Calcul Québec (calculquebec.ca) and Compute Canada (www.computecanada.ca).

REFERENCES

ALMA Partnership, Brogan, C. L., Pérez, L. M., et al. 2015, ApJL, 808, L3, doi: 10.1088/2041-8205/808/1/L3

Andrews, S. M., Huang, J., Pérez, L. M., et al. 2018, ApJL, 869, L41, doi: 10.3847/2041-8213/aaf741

Ansdell, M., Williams, J. P., Trapman, L., et al. 2018, ApJ, 859, 21, doi: 10.3847/1538-4357/aab890

Armitage, P. J. 2018, A Brief Overview of Planet Formation, ed. H. J. Deeg & J. A. Belmonte, 135, doi: 10.1007/978-3-319-55333-7_135

Bai, X.-N., & Stone, J. M. 2010, ApJL, 722, L220, doi: 10.1088/2041-8205/722/2/L220

Bertoldi, F., & McKee, C. F. 1992, ApJ, 395, 140, doi: 10.1086/171638

Birnstiel, T., & Andrews, S. M. 2014, ApJ, 780, 153, doi: 10.1088/0004-637X/780/2/153
Bitsch, B., Morbidelli, A., Johansen, A., et al. 2018, A&A, 612, A30, doi: 10.1051/0004-6361/201731931
Brauer, F., Dullemond, C. P., & Henning, T. 2008, A&A, 480, 859, doi: 10.1051/0004-6361:20077759
Carballido, A., Stone, J. M., & Turner, N. J. 2008, MNRAS, 386, 145, doi: 10.1111/j.1365-2966.2008.13014.x
Carrera, D., Simon, J. B., Li, R., Kretke, K. A., & Klahr, H. 2021, AJ, 161, 96, doi: 10.3847/1538-3881/abd4d9
Chachan, Y., Dalba, P. A., Knutson, H. A., et al. 2022, ApJ, 926, 62, doi: 10.3847/1538-4357/ac3ed6
Chiang, E., & Youdin, A. N. 2010, Annual Review of Earth and Planetary Sciences, 38, 493, doi: 10.1146/annurev-earth-040809-152513
Dittrich, K., Klahr, H., & Johansen, A. 2013, ApJ, 763, 117, doi: 10.1088/0004-637X/763/2/117
Dong, R., & Fung, J. 2017, ApJ, 835, 146, doi: 10.3847/1538-4357/835/2/146
Dong, R., Li, S., Chiang, E., & Li, H. 2017, ApJ, 843, 127, doi: 10.3847/1538-4357/aa72f2
Dullemond, C. P., Birnstiel, T., Huang, J., et al. 2018, ApJL, 869, L46, doi: 10.3847/2041-8213/aaf742
Facchini, S., Birnstiel, T., Bruderer, S., & van Dishoeck, E. F. 2017, A&A, 605, A16, doi: 10.1051/0004-6361/201630329
Flaherty, K. M., Hughes, A. M., Rose, S. C., et al. 2017, ApJ, 843, 150, doi: 10.3847/1538-4357/aa79f9
Gerbig, K., & Laughlin, G. 2022, arXiv e-prints, arXiv:2204.03007. https://arxiv.org/abs/2204.03007
Gerbig, K., Murray-Clay, R. A., Klahr, H., & Baehr, H. 2020, ApJ, 895, 91, doi: 10.3847/1538-4357/ab8d37
Goldreich, P., & Tremaine, S. 1980, ApJ, 241, 425, doi: 10.1086/158356
Hawley, J. F., Gammie, C. F., & Balbus, S. A. 1995, ApJ, 440, 742, doi: 10.1086/175311
Hopkins, P. F. 2015, MNRAS, 450, 53, doi: 10.1093/mnras/stv195
—. 2016, MNRAS, 462, 576, doi: 10.1093/mnras/stw1578
—. 2017, MNRAS, 466, 3387, doi: 10.1093/mnras/stw3306
Hopkins, P. F., & Lee, H. 2016, MNRAS, 456, 4174, doi: 10.1093/mnras/stv2745
Hopkins, P. F., & Raives, M. J. 2016, MNRAS, 455, 51, doi: 10.1093/mnras/stv2180
Hopkins, P. F., Squire, J., & Seligman, D. 2020, MNRAS, 496, 2123, doi: 10.1093/mnras/staa1046
Huang, P., Li, H., Isella, A., et al. 2020, ApJ, 893, 89, doi: 10.3847/1538-4357/ab8199
Johansen, A., Oishi, J. S., Mac Low, M.-M., et al. 2007, Nature, 448, 1022, doi: 10.1038/nature06086
Johansen, A., Youdin, A., & Mac Low, M.-M. 2009, ApJL, 704, L75, doi: 10.1088/0004-637X/704/2/L75
Klahr, H., Pfeil, T., & Schreiber, A. 2018, in Handbook of Exoplanets, ed. H. J. Deeg & J. A. Belmonte, 138, doi: 10.1007/978-3-319-55333-7_138
Kley, W., & Nelson, R. P. 2012, ARA&A, 50, 211, doi: 10.1146/annurev-astro-081811-125523
Kretke, K. A., & Levison, H. F. 2014, AJ, 148, 109, doi: 10.1088/0004-6256/148/6/109
Lambrechts, M., & Johansen, A. 2012, A&A, 544, A32, doi: 10.1051/0004-6361/201219127
Lee, H., Hopkins, P. F., & Squire, J. 2017, MNRAS, 469, 3532, doi: 10.1093/mnras/stx1097
Lin, D. N. C., & Papaloizou, J. 1986, ApJ, 309, 846, doi: 10.1086/164653
Lin, D. N. C., & Papaloizou, J. C. B. 1993, in Protostars and Planets III, ed. E. H. Levy & J. I. Lunine, 749
Lin, J. W., Lee, E. J., & Chiang, E. 2018, MNRAS, 480, 4338, doi: 10.1093/mnras/sty2159
Lin, M.-K. 2014, MNRAS, 437, 575, doi: 10.1093/mnras/stt1909
Long, F., Andrews, S. M., Rosotti, G., et al. 2022, arXiv e-prints, arXiv:2203.16735. https://arxiv.org/abs/2203.16735
Morbidelli, A. 2020, A&A, 638, A1, doi: 10.1051/0004-6361/202037983
Moseley, E. R., Squire, J., & Hopkins, P. F. 2019, MNRAS, 489, 325, doi: 10.1093/mnras/stz2128
Nakagawa, Y., Sekiya, M., & Hayashi, C. 1986, Icarus, 67, 375, doi: 10.1016/0019-1035(86)90121-1
Onishi, I. K., & Sekiya, M. 2017, Earth, Planets and Space, 69, 50, doi: 10.1186/s40623-017-0637-z
Ono, T., Muto, T., Takeuchi, T., & Nomura, H. 2016, ApJ, 823, 84, doi: 10.3847/0004-637X/823/2/84
Ormel, C. W. 2017, in Astrophysics and Space Science Library, Vol. 445, Formation, Evolution, and Dynamics of Young Solar Systems, ed. M. Pessah & O. Gressel, 197, doi: 10.1007/978-3-319-60609-5_7
Ormel, C. W., & Klahr, H. H. 2010, A&A, 520, A43, doi: 10.1051/0004-6361/201014903
Paardekooper, S. J., & Mellema, G. 2006, A&A, 453, 1129, doi: 10.1051/0004-6361:20054449
Pan, L., Padoan, P., Scalo, J., Kritsuk, A. G., & Norman, M. L. 2011, ApJ, 740, 6, doi: 10.1088/0004-637X/740/1/6
Pinilla, P., Birnstiel, T., Ricci, L., et al. 2012, A&A, 538, A114, doi: 10.1051/0004-6361/201118204
Pinilla, P., & Youdin, A. 2017, Particle Trapping in Protoplanetary Disks: Models vs. Observations, ed. M. Pessah & O. Gressel, Vol. 445, 91, doi: 10.1007/978-3-319-60609-5_4

Pinte, C., Dent, W. R. F., Ménard, F., et al. 2016, ApJ, 816, 25, doi: 10.3847/0004-637X/816/1/25

Rafikov, R. R. 2002, ApJ, 572, 566, doi: 10.1086/340228

Scott, D. 2015, Multivariate Density Estimation: Theory, Practice, and Visualization, Wiley Series in Probability and Statistics (Wiley). https://books.google.com/books?id=XZ03BwAAQBAJ

Seligman, D., Hopkins, P. F., & Squire, J. 2019, MNRAS, 485, 3991, doi: 10.1093/mnras/stz666

Simon, J. B., Armitage, P. J., Li, R., & Youdin, A. N. 2016, ApJ, 822, 55, doi: 10.3847/0004-637X/822/1/55

Squire, J., & Hopkins, P. F. 2020, MNRAS, 498, 1239, doi: 10.1093/mnras/staa2311

Su, K.-Y., Hopkins, P. F., Hayward, C. C., et al. 2017, MNRAS, 471, 144, doi: 10.1093/mnras/stx1463

Taki, T., Fujimoto, M., & Ida, S. 2016, A&A, 591, A86, doi: 10.1051/0004-6361/201527732

Tazzari, M., Testi, L., Ercolano, B., et al. 2016, A&A, 588, A53, doi: 10.1051/0004-6361/201527423

Tobin, J. J., Sheehan, P. D., Megeath, S. T., et al. 2020, ApJ, 890, 130, doi: 10.3847/1538-4357/ab6f64

Trapman, L., Facchini, S., Hogerheijde, M. R., van Dishoeck, E. F., & Bruderer, S. 2019, A&A, 629, A79, doi: 10.1051/0004-6361/201834723

Tripathi, A., Andrews, S. M., Birnstiel, T., et al. 2018, ApJ, 861, 64, doi: 10.3847/1538-4357/aac5d6

Weidenschilling, S. J. 1977, MNRAS, 180, 57, doi: 10.1093/mnras/180.2.57

Whipple, F. L. 1972, in From Plasma to Planet, ed. A. Elvius, 211

Youdin, A. N., & Goodman, J. 2005, ApJ, 620, 459, doi: 10.1086/426895

Youdin, A. N., & Lithwick, Y. 2007, Icarus, 192, 588, doi: 10.1016/j.icarus.2007.07.012

Zhu, Z., Nelson, R. P., Dong, R., Espaillat, C., & Hartmann, L. 2012, ApJ, 755, 6, doi: 10.1088/0004-637X/755/1/6